Cyclic Inelastic In-Plane Flexural Behavior of Concrete-Filled, Sandwich Steel Panel Walls with Different Cross-Section Properties

ERKAN POLAT and MICHEL BRUNEAU

ABSTRACT

Flexure-dominated, concrete-filled, sandwich steel plate walls (CFSSP-Walls) walls have been studied experimentally by various researchers using a small number of cross-sections and wall aspect ratios. Using these past results to calibrate finite element models, the expected behavior of CFSSP-Walls having different geometries and cross-section properties is investigated here using finite element approaches. Results obtained show that the plastic moment can be used to conservatively predict maximum flexural strength in all cases considered and to provide valuable insights into stress and strain demands at various points during nonlinear response. Results also provide quantification of the contribution of concrete infill on the wall effective stiffness, assessment of wall ductility having a failure criteria based on cumulative plastic strain at steel plate fracture, and effect of wall flange width on the wall behavior of T-shaped sections.

Keyword: steel plate walls, CFSSP, effective stiffness, plate fracture.

INTRODUCTION

Concrete-filled, sandwich steel panel walls (CFSSP-Walls) have been the subject of extensive research in recent years, with an emphasis on their potential application in nuclear power plants or high rises (e.g., Oduyemi and Wright, 1989; Wright et al., 1991a, 1991b; Xie and Chapman, 2006; Eom et al., 2009; Ramesh, 2013; Zhang et al., 2014; Sener and Varma, 2014; Varma et al., 2014; Epackachi et al., 2014; Sener et al., 2015; Epackachi et al., 2015; Booth et al., 2015; Kurt et al., 2016; Seo et al., 2016; Alzeni and Bruneau, 2017; Polat and Bruneau, 2017). Referred to as "composite plate shear walls—concrete filled (C-PSW/CF) by the AISC *Seismic Provisions* (AISC, 2016), and steel concrete (SC) walls in some of the above-cited publications, these walls consist of dual-steel-plate "sandwiching" a concrete infill. Their appeal over traditional reinforced concrete walls mainly lies in their rapid site construction (because the steel plates can provide temporary formwork and can resist alone some of the construction loads), their high composite strength, and their smaller thickness (resulting in greater leasable floor space in high-rise applications). Experimental research has demonstrated that CFSSP-Walls can be highly ductile in flexure (e.g., Eom et al., 2009; Alzeni and Bruneau, 2014), as long as the ties that connect the steel plates are properly designed (Bowerman et al., 1999; Ramesh, 2013) and plate buckling only occurs after development of the plastic moment.

Design requirements for CFSSP-Walls specified by the AISC *Seismic Provisions* (AISC, 2016) are based on results from a limited number of tests, largely conducted on planar walls and for a small number of cross-section aspect ratios. While further testing is desirable, and anticipated to occur in the future, finite element analysis can be used to investigate the expected behavior of other CFSSP-Wall configurations and aspect ratios and to determine if satisfactory behavior is also obtained in these other cases, possibly providing enhanced confidence over a broader range of applicability. This can be done as long as the finite element models used for this purpose have been developed and calibrated against prior CFSSP-Wall experimental results. Such development and calibration has been done by Polat and Bruneau (2017), using experimental results from Alzeni and Bruneau (2014, 2017). The finite element models developed in that study were able to replicate the cyclic inelastic in-plane flexural behavior of the CFSSP-Wall up to failure and to capture the mechanisms that control this behavior (namely, in this case, steel yielding and strain hardening, concrete cracking and confinement, global strength and stiffness degradation, plastic local buckling, pinching of the hysteresis loops, and cumulative-plastic strains prior to fracture). In the process, suitable material models, element types, element sizes, and

Erkan Polat, Ph.D., Department of Civil, Structural and Environmental Engineering, University at Buffalo, State University of New York, Buffalo, NY. E-mail: erkanpol@buffalo.edu (corresponding)

Michel Bruneau, Professor, Department of Civil, Structural and Environmental Engineering, University at Buffalo, State University of New York, Buffalo, NY.

Table 1. Cross-Sectional Properties of the CFSSP-Walls						
Wall Designation	W, in.	b, in.	t_s, in.	t_c, in.	S, in.	d_{in}, in.
CFSSP-B1	44	30	5/16	6	8	8
CFSSP-B2	44	30	5/16	6	12	8
CFSSP-NB1	48.625	40	5/16	8	8	8
CFSSP-NB2	48.625	40	5/16	8	12	8

contact models were identified. This study also accounted for the flexibility induced by the footing at the wall base (as part of the test set-up) by explicitly modeling it. Furthermore, it was demonstrated (Polat and Bruneau, 2017; Alzeni and Bruneau, 2014, 2017) that the ultimate flexural strength of these planar walls can be conservatively predicted by equations based on simple plastic theory that assume uniform steel yield strength, F_y, and uniform compressive concrete strength. f'_c.

Here, using the finite element model developed and validated by Polat and Bruneau (2017), a number of CFSSP-Walls having different cross-section properties are investigated. For this purpose, analysis of the CFSSP-Walls experimentally tested by Alzeni and Bruneau, but without their footing, was first conducted to establish a basis for all comparisons; this was done because only fixed-base walls results are of interest here (i.e., to ensure that only wall behavior is compared here because the footings were only needed for experimental purposes and differ from how wall-base connection would be accomplished in actual applications). Analysis results from these fixed-base wall models are also used to predict the contribution of infill concrete on the wall effective lateral stiffness. Then presented are the results from a parametric study considering many cross-section aspect ratios and properties, conducted to assess the adequacy of the simple plastic moment equations to predict the results obtained from the finite element models. Finally, the finite element model is used to investigate the behavior of a T-shaped CFSSP-Wall tested by Eom et al. (2009), and a modified version of that wall having a much wider flange.

Note that while much research has also been conducted on shear (or shear-flexure) in-plane behavior of CFSSP-Walls having low aspect ratio ranging from 0.6 to 1.0 (Varma et al., 2014; Zhang et al., 2014; Epackachi et al., 2015, Kurt et al., 2016; Seo et al., 2016), the focus here is on flexure-dominated CFSSP-Walls that are expected to yield in flexure because this is the case in high-rise applications.

CFSSP-WALLS AND FINITE ELEMENT MODELING

Figure 1 illustrates the cross-section of the CFSSP-Walls tested by Alzeni and Bruneau (2014, 2017) and used by Polat and Bruneau (2017) to develop and calibrate the finite element model; it also shows the plastic stress distributions and closed-form equations (provided in AISC *Seismic Provisions* Eqs. C-H7-2 through C-H7-6), used to calculate the plastic flexural strength, M_p, of the walls. Table 1 presents the values of the parameters that define the cross-sections shown in Figure 1. Note that tie spacing, S, of these walls was selected based on AISC *Seismic Provisions* Equation H7-1 ($S = 1.8 t_S \sqrt{E/F_y}$) to ensure steel plate yielding before plate buckling. These walls were (and will be) referred as B1, B2 (group B) and NB1, NB2 (group NB) as shown in Figure 1. Note that the ends of group B walls consisted of round HSS columns, whereas half-round HSS columns were used for group NB walls. The walls were cantilever type, and the height of the specimens above the footing was 120 in.

The finite element study of the walls was performed using LS-Dyna (LSTC, 2015). Following is a brief description of the element types, material models, and contact models used in the finite element analyses performed by Polat and Bruneau (2017). Note that the work presented here (for the parametric study of CFSSP-Walls and for the study on T-shaped walls) follows the same modeling approach.

The concrete infill was modeled using an eight-node, constant stress solid element (*solid 1*) with reduced integration and the *Winfrith_concrete* model (Material 084/085 in LS-Dyna). The size of the solid elements was 1×1×1 in. The steel sandwich panels and HSS were modeled using four-node, fully integrated shell elements (*shell 16*) with Belytschko-Tsay shell formulation with three integration points through thickness and the *plastic_kinematic* (Material 3 in LS-Dyna) bi-linear material model with kinematic hardening. The shell elements were 1×1 in. and had the thickness of steel panels. The ties that extend between the dual plates (needed to develop composite action and transfer shear forces along the steel-concrete interface) were modeled using two-node beam elements (*beam 1*) with Hughes-Liu beam formulation with two integration points and the *plastic_kinematic* material model. Note that the average uniaxial tension coupon test data reported in Alzeni and Bruneau (2014) were used for the steel material model properties, and the average uniaxial compression test data were used for the concrete material model properties. As reported in Polat and Bruneau (2017), the elastic modulus used in

the simulations was 29,800 ksi (205,463 MPa) for the steel web and 27,500 ksi (189,605 MPa) for the HSS. For the web plate (WP) and HSS, as far as the other bi-linear steel model parameters were concerned, $Fy_{\_WP}$ of 62 (427), 64 (441), 61 (420), and 63 ksi (434 MPa); E_{T_WP} of 100 (689), 100 (689), 80 (551), and 110 ksi (758 MPa); $Fy_{\_HSS}$ of 56 (386), 56 (386), 52 (358), and 51 ksi (351 MPa); and E_{T_HSS} of 80 (551), 60 (413), 50 (344), and 50 ksi (344 MPa) were used for the models B1, B2, NB1, and NB2, respectively, where Fy is the yield strength and E_T is the tangent modulus after yielding. Similarly, the average concrete compressive strengths were 7.1 (50), 4.8 (33), 6.9 (47), and 6.8 ksi (47 MPa) for B1, B2, NB1, and NB2.

The interaction between the steel sandwich panels and the infill concrete was defined using the *automatic_ surface_to_surface_mortar* contact model with static interface friction coefficient of 0.3 and increased contact stiffness [the work substantiating the choice of this contact model is presented in Polat and Bruneau (2017)]. The displacement controlled drift reversals were modeled with a single cycle per drift amplitude, as opposed to the multiple cycles per drift amplitude in the actual tests. In the numerical simulation, displacement histories with user-defined time steps was used to apply the displacement history; this was done to define the time intervals of the numerical integration for the implicit solution procedure in the program and to expedite
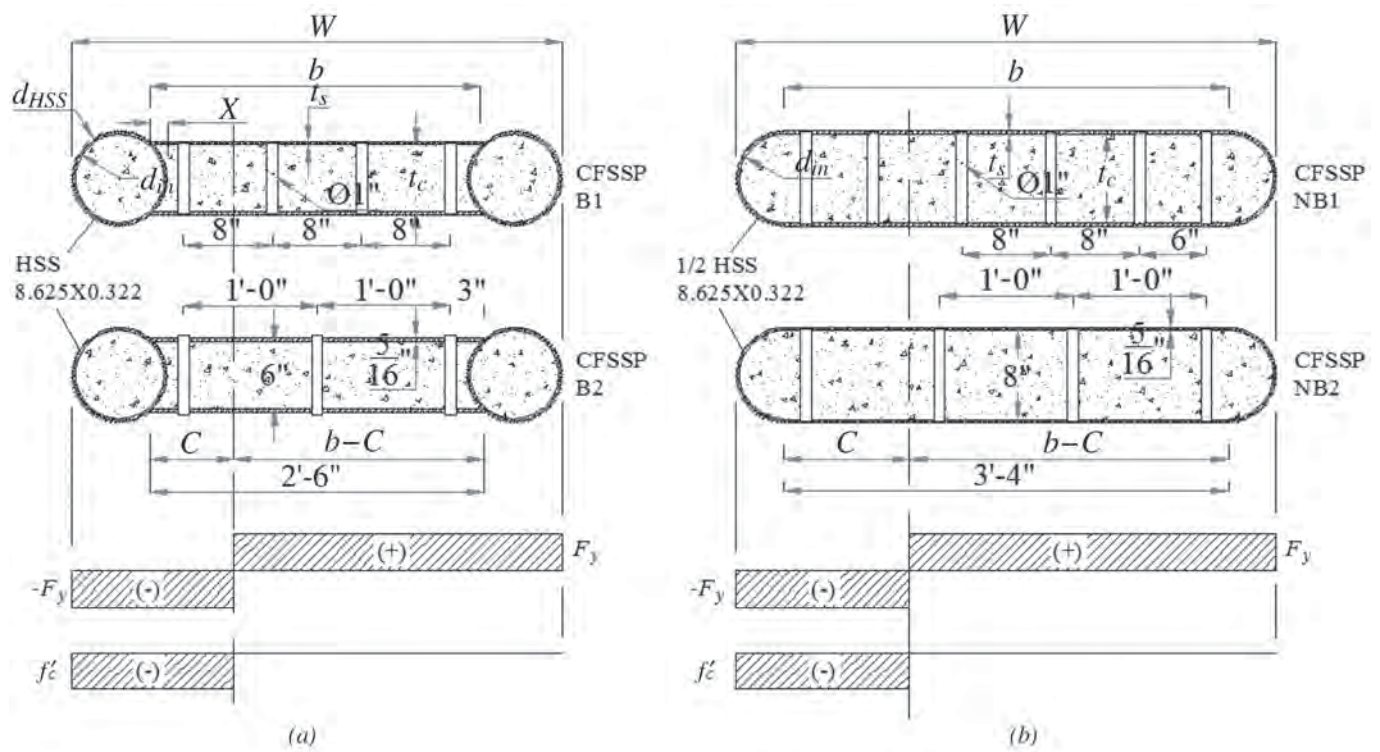
CFSSP	*Depth of Compression Zone, C, and Plastic Flexural Strength, M_p
NB	$M_p = 0.5A_{HSS}F_{yHSS}\left(\dfrac{2d_{HSS}}{\pi}+b\right) + [b^2 + 2C^2 - 2Cb]t_sF_{yweb} + \left(\dfrac{2d_{in}^2 + 3\pi d_{in}^2 C}{24} + \dfrac{C^2 t_c}{2}\right)f_c'$ $C = \dfrac{2bt_sF_{yweb} - 0.125(\pi d_{in}^2)f_c'}{4t_sF_{yweb} + t_cf_c'}$
B	$M_p = A_{HSS}F_{yHSS}(b - 2X + d_{HSS}) + [b^2 + 2C^2 - 2Cb]t_sF_{yweb}$ $\qquad + [0.25\pi d_{in}^2(0.5d_{HSS} + C - X) + 0.33Xt_c(C - 0.67X) + 0.5t_c(C - X)^2]f_c']$ $X = 0.5\left(d_{in} - \sqrt{d_{in}^2 - t_c^2}\right)$ $C = \dfrac{2bt_sF_{yweb} + (0.67Xt_c - 0.25\pi d_{in}^2)f_c'}{4t_sF_{yweb} + t_cf_c'}$

Fig. 1. *Cross-sectional dimensions of CFSSP-Walls, stress blocks, and closed-form solutions used to calculate plastic flexural strength,* M_p, *of CFSSP-Walls: (a) group B walls; (b) group NB walls (Polat and Bruneau, 2017).*

simulation run time and increase convergence, as defined in Polat and Bruneau (2017).

The implementation of the steel material model (material 3) in LS-Dyna is based on the formulation by Kreig and Key (1976) (see also Hallquist, 2006). In this material model, the yield criteria is based on the von Mises (also known as effective stress) interaction of stresses. The definition of effective stress and effective plastic strain (in tensorial notation) is given by the following equations:

$$\sigma_{VM} = \frac{1}{\sqrt{2}} \left[(\sigma_x - \sigma_y)^2 + (\sigma_y - \sigma_z)^2 + (\sigma_z - \sigma_x)^2 + \right.$$
$$\left. 6 (\sigma_{xy}^2 + \sigma_{yz}^2 + \sigma_{zx}^2) \right]^{\frac{1}{2}} \tag{1}$$

$$\varepsilon_{eff}^p = \int_0^t \left[2/3 \left(\dot{\varepsilon}_{ij}^p \dot{\varepsilon}_{ij}^p \right) \right]^{\frac{1}{2}} dt \tag{2}$$

where σ_x, σ_y, σ_z are normal stresses; σ_{xy}, σ_{yz}, σ_{zx} are shear stresses in a three-dimensional continuum body; and $\dot{\varepsilon}_{ij}^p$ is the plastic component of the rate of deformation tensor. The effective plastic strain (grows whenever the material is actively yielding) was used in this study to determine the initiation and propagation of the fracture critical region of the steel section.

Note that the Winfrith concrete model in LS-Dyna (material 85) considers smeared cracking and has a crack formulation (Wittmann et al., 1988) that considers aggregate size, concrete compressive strengths, loading rates, cement-to-water ratios, and test specimen size (Schwer, 2011). The material model is capable of simulating the opening and closing of the concrete cracks under tensile and compressive stresses, respectively, which is essential to capture the pinching effect observed in the wall's hysteresis curves, as effectively demonstrated by Goto et al. (2010) and Imani and Bruneau (2014) for concrete-filled steel tube columns. Schwer (2011) explains the plasticity models, the strain rate formulation, and tensile cracking options of this material model. Note that the Winfrith concrete model has also been used by Epackachi et al. (2015) and Kurt et al. (2015) in the simulation of SC composite shear walls with aspect ratios of 0.6 to 1.0.

FINITE ELEMENT ANALYSES OF FIXED-BASE CFSSP-WALL MODELS

Analyses of the CFSSP-Walls, including foundation flexibility by Polat and Bruneau (2017), showed that the force distribution inside the wall footing is rather complex. Explicit modeling of the wall footing introduced flexibility at the wall base due to its deformation under shear and moment forces from the embedded part of the wall under wall deformation. Base flexibility may alter the wall response in a number of ways, the ultimate drift ratio at failure of wall is increased due to additional drift that stems from the base rotation introduced within the footing, and steel plate buckling likewise occurs at larger drifts due to reduced axial strains at a
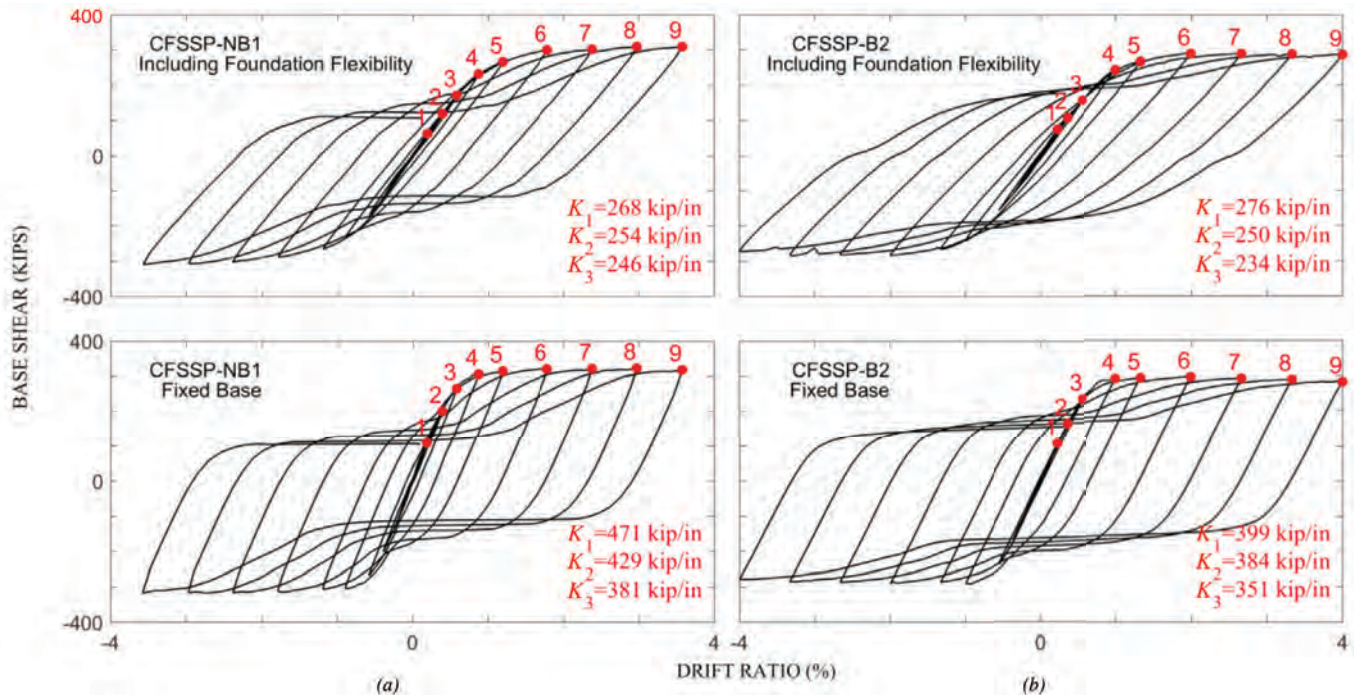

Fig. 2. Comparison of initial wall stiffness of LS-Dyna models with and without foundation flexibility: (a) CFSSP-NB1; (b) CFSSP-B2.

particular drift. Wall displacement ductility (given by the ratio between ultimate wall drift and yield drift) may also be effected, to a lesser degree.

To illustrate the effect of foundation flexibility on the wall response, Figure 2 shows a comparison of hysteretic curves of selected CFSSP-Walls (NB1 and B2) analyzed with and without their foundation. [Note that comparisons for the wall models NB2 and B1 were not included due to space concerns; however, model B2 was intentionally chosen because this model was also used by Polat and Bruneau (2017) to obtain effective plastic strain values for steel plate fracture for specimen with flexible foundation; similar work is also performed here, but for the fixed-base model of B2.] Initial wall stiffnesses from each curve are reported using secant stiffness values at the first three peak positive-drift locations shown in the figures (peak positive drift locations are denoted with numbers from 1 to 9). Stiffness values

(shown on the figures) indicate that fixed-base models are approximately 1.4 to 1.80 times stiffer than their counterpart with base flexibility.

To compare the effect of wall stiffness on the axial strain demand, Figure 3 shows the lateral force versus axial strain hysteresis of these walls obtained from the outermost steel element at the wall base. This demonstrates that axial strain amplitudes of the fixed-base model are much larger than those of the model with foundation flexibility at the same drift amplitude. Note that for the fixed-base wall models of the CFSSP-NB1 and B2 walls, steel plate local buckling develops at a drift amplitude of 1.20 and 1.33%, respectively [whereas it was 1.80 and 2.00% for the same walls with base flexibility, as shown in Polat and Bruneau (2017)]. The tensile-axial-strains of these models at the onset of steel plate buckling were 0.024 in./in. and 0.031 in./in., respectively, for CFSSP NB1 ($S/t_s = 25.6$) and B2 ($S/t_s = 38.4$).
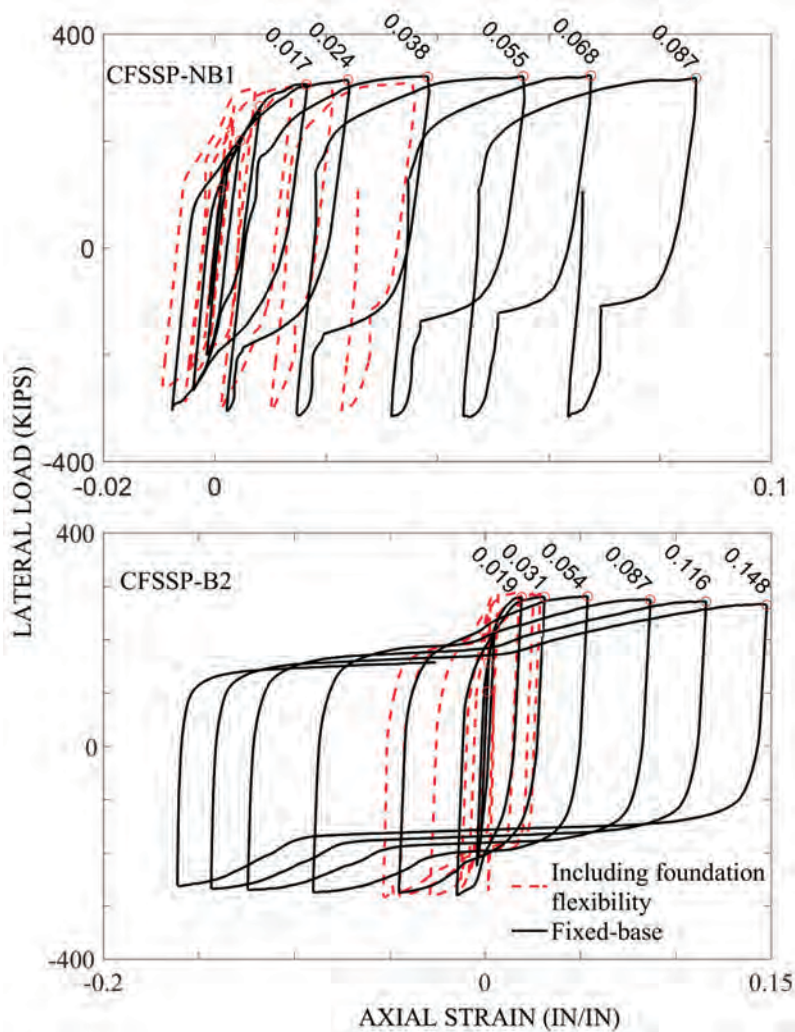

Fig. 3. Comparison of lateral load versus steel strain relationships for CFSSP-NB1 for fixed base and including foundation flexibility.

Figures 4 and 5 show the lateral force–drift ratio hysteresis of the fixed-base models for the group B and NB specimens, including relative contributions of the steel and concrete components of the cross-section to the total hysteretic curves. The base shear (denoted as V_p) at which the walls attain their plastic flexural strength (see Figure 1 for M_p), is also shown ($V_p = M_p/H$, where M_p is based on simple plastic theory and H is the wall height). Figures 4 and 5 reveal that the steel section accounts for about 80% of the wall strength, which is consistent with the design values recommended by Alzeni and Bruneau (2014). These figures also indicate a reduction of the flexural strength of steel skin as a result of steel plate buckling after about 1.0% drift ratio. [Note that the experimental measurement and findings of the CFSSP-Walls reported in Alzeni and Bruneau (2014, 2017) showed that some minor strength degradation occurred post-buckling; the main strength degradation of the specimens mostly occurred following steel plate fracture. Modeling of steel plate fracture in an explicit manner is a complex issue to be investigated in future research.] The reduction of steel flexural strength, due to steel plate buckling, is more severe for the group NB wall models (~45% reduction for NB1 and ~60% for NB2) than for the group B wall models (~20% reduction for B1 and ~30% for B2). Note that while Polat and Bruneau (2017) provide stress distribution plots for the CFSSP-Walls considering foundation flexibility to match that of the specimens tested, such plots are not provided here for the fixed-base walls considered in this paper due to space limitations. However, the stress distribution of the planar CFSSP-Walls [provided in Polat and Bruneau (2017)] does not indicate concrete crushing (which is defined to occur when both degradation in the strength contributed by concrete and reduction in maximum concrete stresses occur simultaneously), which is consistent with the CFSSP-Wall hysteresis shown in Figures 4 and 5.

Note that the lateral force-drift hysteresis of concrete shows that stiffness and strength contribution of concrete is delayed under subsequent drift amplitudes, following the drift amplitude of 1.0%. This is a result of the opening and closing of the horizontal tensile cracks forming in concrete under reversed cyclic drifts and the development of higher crack widths or formation of new cracks along the uncrack region of the concrete under increased drift amplitudes, which can be explained as follows. Under cyclic loading, in a given displacement direction, residual tensile strains develop in the steel skin, which results in elongations in the steel section and horizontal tensile cracking in the infill concrete. Under reversal of displacements, while the steel section that has residual tensile strains can still resist compressive stresses as well as shear stresses, the cracked
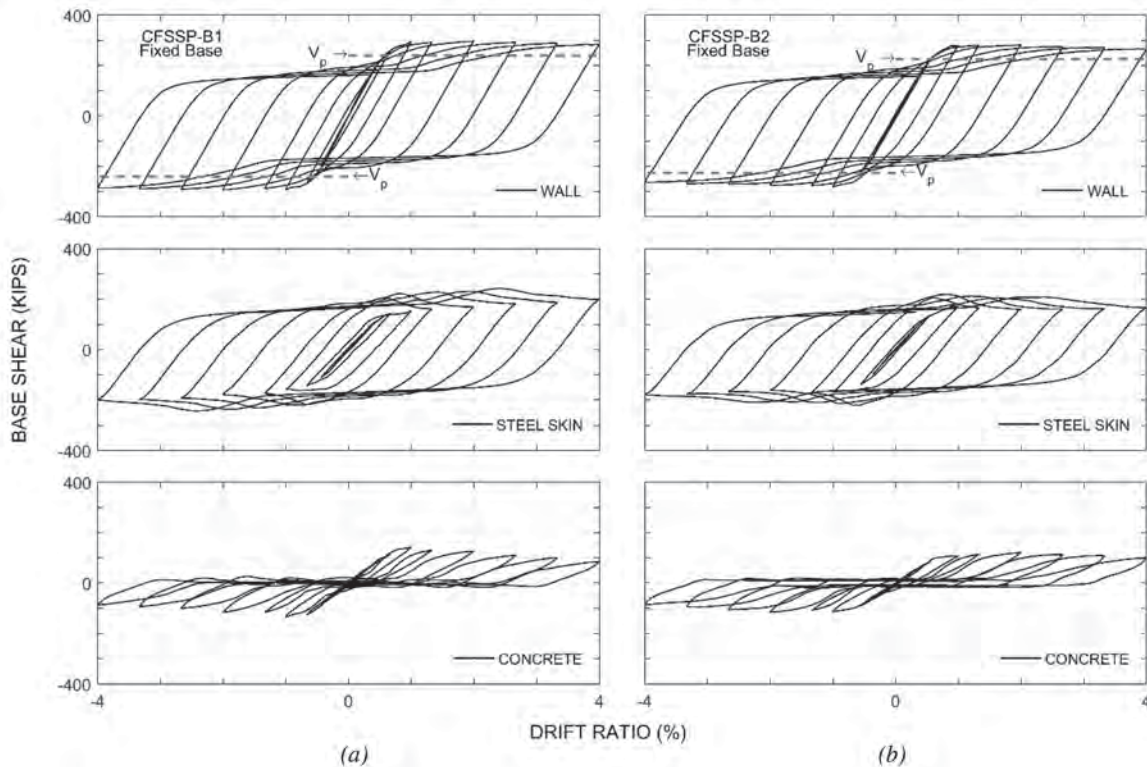

Fig. 4. Hysteresis curves of the LS-Dyna model for group B walls: (a) CFSSP-B1; (b) CFSSP-B2.

concrete does not resist any normal and shear stresses until the tensile cracks are closed. During the opening and closing of the horizontal tensile cracking, shear resistance is mainly provided by the steel section of the wall, while limited contribution comes from the concrete section. The relative contribution of concrete increases with closure of the horizontal tensile cracks following the development of steel plate buckling.

Contribution of Concrete to Equivalent Effective Stiffness of CFSSP-Walls

Equivalent effective stiffness is typically represented as the sum of the stiffness contributions from the steel and concrete as given by Equation 3 (AISC, 2016). In Equation 3, I_S and I_C are the gross moment of inertia of the steel and concrete parts of the CFSSP-Wall cross-section, respectively. C_3 is a reduction factor accounting for the cracking of concrete.

$$EI_{eff} = E_S I_S + C_3 E_C I_C \qquad (3)$$

Alzeni and Bruneau (2014) recommended a C_3 factor of 0.4 based on results of finite element analyses conducted using ABAQUS (SIMULIA, 2012). Although, those models were calibrated based on flexural test results, Polat and

Bruneau (2017) showed that better results could be obtained using the Winfrith concrete model (available in LS-Dyna, not in ABAQUS, at the time of this writing), compared to those obtained using the concrete damage plasticity model in ABAQUS (Hibbett et al., 1998), particularly when it came to replicate pinching of the hysteresis loops and peak strength at each cycle of loading.

The availability of finite element results, using a model calibrated on the experimental results and then equivalently converted into a fixed-base model, makes it possible to assess the value of C_3 in Equation 3 for this structural system. Assuming the wall acting as a cantilever beam, with a tip lateral deflection of $\Delta = PL^3/3EI$ (for a beam length L, flexural rigidity EI, and unit load P at the tip), C_3 can be calculated using the stiffness values obtained from the finite element analyses results by replacing EI in the equation with EI_{eff}. In this calculation, the effective flexural rigidity of the LS-Dyna models, EI_{eff}, the peak displacement, Δ, and the corresponding load, P, at the first loading cycle were used. The calculated EI_{eff} and corresponding C_3 values for each CFSSP-Walls are given in Table 2. The values for C_3 are between 0.30 and 0.45 and are in relative agreement with that recommended ($C_3 = 0.4$) by Alzeni and Bruneau (2014).
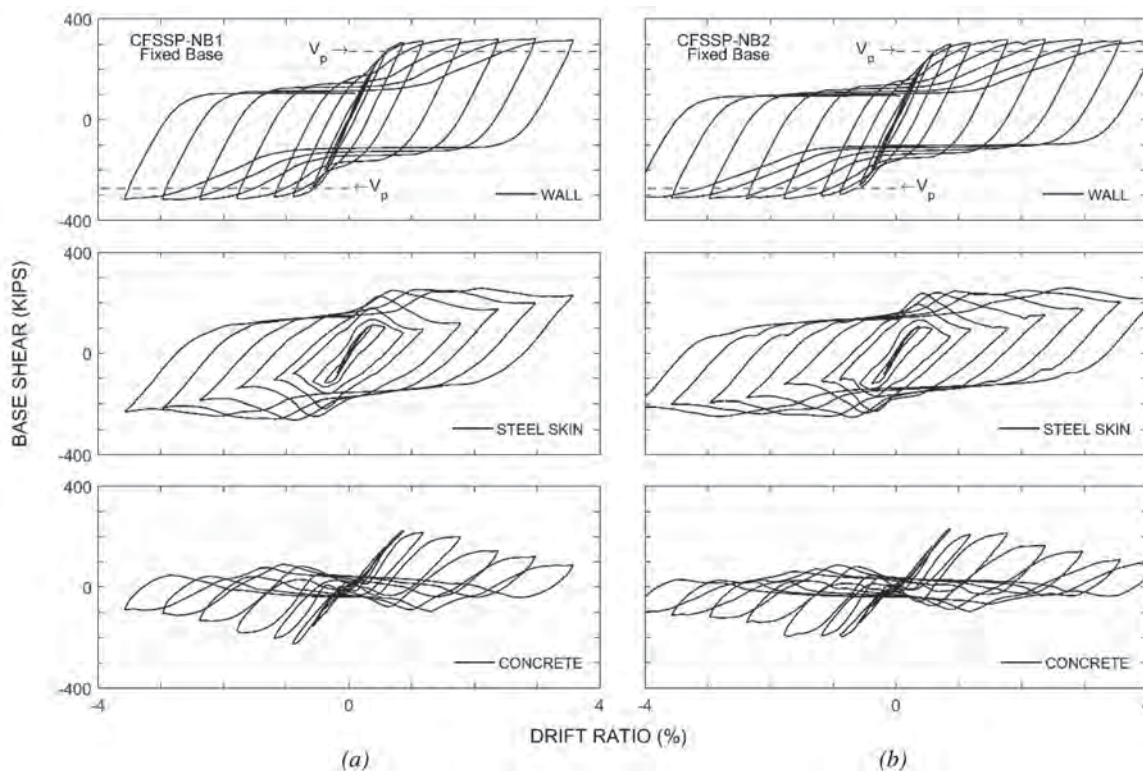

Fig. 5. Hysteresis curves of the LS-Dyna models for group NB walls: (a) CFSSP-NB1; (b) CFSSP-NB2.

Table 2. C_3 Values for Each of the LS-Dyna Models for CFSSP-Walls		
CFSSP-Wall	***EI*eff**	***C*₃, FE Model**
CFSSP-NB1	271447306	0.37
CFSSP-NB2	261590952	0.31
CFSSP-B1	232520184	0.44
CFSSP-B2	232018928	0.43

Yielding and Prediction of Failure Drift Ratio for a Fixed-Base CFSSP-Wall

As noted before, the steel plates yielding was modeled using the von Mises yield criteria, which is a combination of three-dimensional normal and shear stresses. Polat and Bruneau (2017) showed that the uniaxial yield strength of the steel skin at the wall boundaries is increased under tension and decreased under compression (as a result of the von Mises' relationship describing interaction between stresses on the yield surface).

Furthermore, although the numerical models do not consider material damage within their hysteretic formulations, a failure criteria can be established for the steel material model by setting a failure cumulative plastic strain limit, such that if this value is exceeded, elements using this material model are eroded. Polat and Bruneau (2017) determined this limit by correlating finite element and experimental results at drift when fracture was observed to occur the for CFSSP-B2 wall. Figures 6 and 7 show the von Mises stress and plastic strain contours of the bottom one-third of the steel skin of the B2 and NB1 wall models, which illustrates yielding and damage-prone regions of the steel skin across the wall base. Figures 6b and 7b show that effective plastic strains are higher in regions where local buckling of steel skin takes place. Therefore, cumulative plastic strain histories obtained from the failure critical element of this buckling region of the steel skin were used to predict the failure drift ratio of the fixed base wall model of CFSSP-B2.

Polat and Bruneau (2017) reported effective plastic strain histories of the fracture critical element for the CFSSP-B2 model with base flexibility. The failure strain values for the finite element model, corrected to correspond to the plastic strain values for the actual specimens subjected to more cycles than the finite element models, were obtained by calculating the plastic strain values at the drift where steel skin fracture was observed to initiate in the actual specimen. The reported plastic strain was 1.40–1.45 from the numerical model under single-cycle loading, and the corrected cumulative plastic strain value for the actual specimen was 2.60 under multiple-cycle loading per drift level. Using the corrected plastic strain for the actual specimen, failure drift of the fixed-base numerical model was determined. Table 3 presents the history of the cumulative plastic strain values of the fracture critical element of the numerical model at various drifts. From the table, the drift level at which this element attain the failure strain is found to be 3.33%.
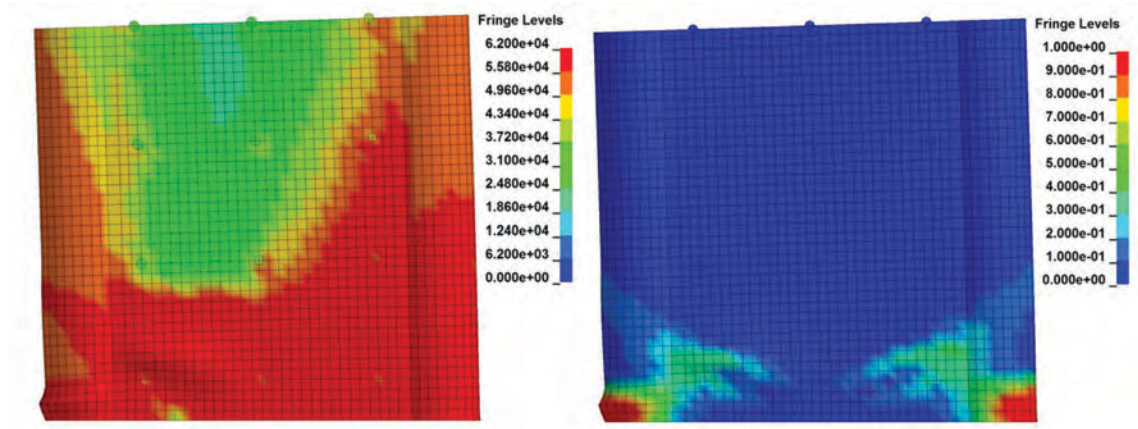

Fig. 6. Von Mises yield stress (a) and effective plastic strain (b) contours of the LS-Dyna model for CFSSP-B2 at 3.33% drift.

Drift Ratio (%)	Cycle Order (i)	Cycle for Each Drift (n)	Cumulative Plastic Strain (PS) LS-Dyna (single cycle)	$PS_{i+1} - PS_i$	$n \times$ $PS_{i+1} - PS_i$	$\sum n \times$ $(PS_{i+1} - PS_i)$
0.23	1	3	0	0	0	0
0.36	2	3	0.0002	0.0002	0.0006	0.0006
0.56	3	3	0.0042	0.004	0.012	0.0126
1.00	4	3	0.0281	0.0239	0.0717	0.0843
1.33	5	3	0.1134	0.0853	0.2559	0.3402
2.00	6	2	0.318	0.2046	0.4092	0.7494
2.67	7	2	0.7432	0.4252	0.8504	1.5998
—	—	*1.5*	*1.4168*	*0.6736*	*1.0104*	*2.6102*
3.33	8	2	1.4168	0.6736	1.3472	3.9574
						$\sum PS = 2.61$

Table 3. Effective Plastic Strain Values for the Fixed-Base CFSSP-B2 Wall Model (failure strain defined by $\sum PS$)

PARAMETRIC STUDY

Finite element analysis was then conducted, using the preceding models, to investigate the possible in-plane behavior of wall configurations similar to the tested CFSSP-NB (i.e., without full HSS boundary elements) but having cross-section geometries different than those considered in the experimental program conducted by Alzeni and Bruneau (2014). The scope of the parametric study was limited to only cover the following aspects:

1. The D/t_s ratio, which is the ratio between the diameter of the HSS part of the cross-section and its thickness, taken as $0.076\ E/F_y$ in addition to the value of $0.044E/F_y$ used in the experiments.

2. The S/t_s ratio, which is the ratio between the tie-bars spacing and the thickness of the skin plate, taken as an arbitrary value of 50 here in addition to the S/t_s ratio of 25.6 and 38.4 used in the experiments.

3. The t_c/b ratio, which is the ratio between the thickness of the concrete and the length of the steel web, with values of 0.1, 0.4, 0.57 and 0.80 considered in addition to 0.2 used in the tested CFSSP-NB wall.

Figure 8 illustrates the cross-section of the walls considered in this parametric study. Table 4 provides the corresponding values for the wall dimensions. Note that to keep the wall aspect ratio similar to the original wall tested (~2.50), the walls with reduced plate widths were reduced in height (i.e., with a wall height of 70 in. for NB-0.4b, 55 in. for NB-0.57b, and 45 in. for NB-0.8b).

Figure 9 shows the lateral load–drift hysteresis of these walls, including the relative contributions from the steel skin
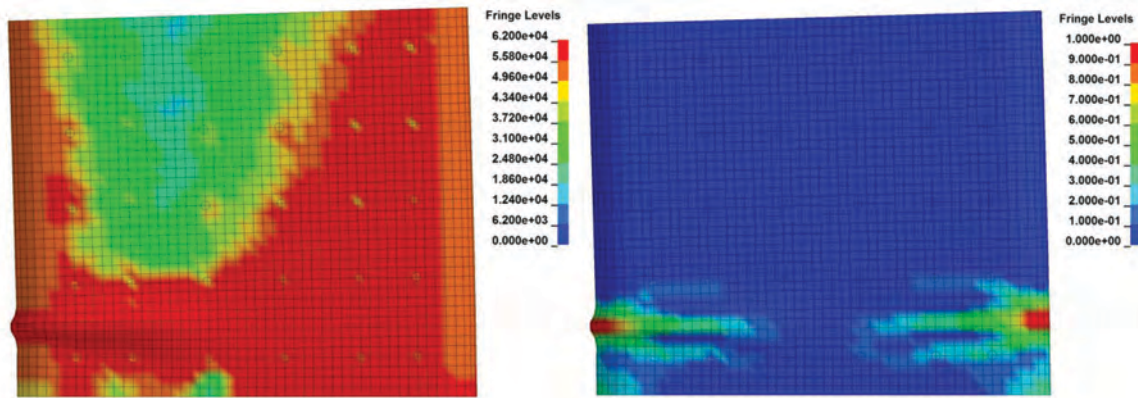

Fig. 7. Von Mises yield stress (a) and effective plastic strain (b) contours of the LS-Dyna model for CFSSP-NB1 at 3.00% drift.

Table 4. Wall Parameters Considered in Parametric Study											
CFSSP Model	D/t_s	S/t_s	t_c, in.	b, in	t_c/b	Wall Height, in.	Aspect Ratio	Web Thickness, in.	HSS Diameter, in.	HSS Thickness, in.	Design Parameter Investigation
NB-D/t_s	44.8	25.6	8	40	0.20	120	2.47	5/16	8.3125	5/32	D/t
NB-S/t_s	25.52	51.2	8	40	0.20	120	2.47	5/16	8.3125	5/16	S/t
NB-0.1b	25.52	25.6	4	40	0.10	120	2.70	5/16	4.3125	5/32	t_c
NB-0.4b	25.52	25.6	8	20	0.40	70	2.45	5/16	8.3125	5/16	t_c
NB-0.57b	25.52	25.6	8	14	0.57	55	2.43	5/16	8.3125	5/16	t_c
NB-0.8b	25.52	25.6	8	10	0.80	45	2.42	5/16	8.3125	5/16	t_c
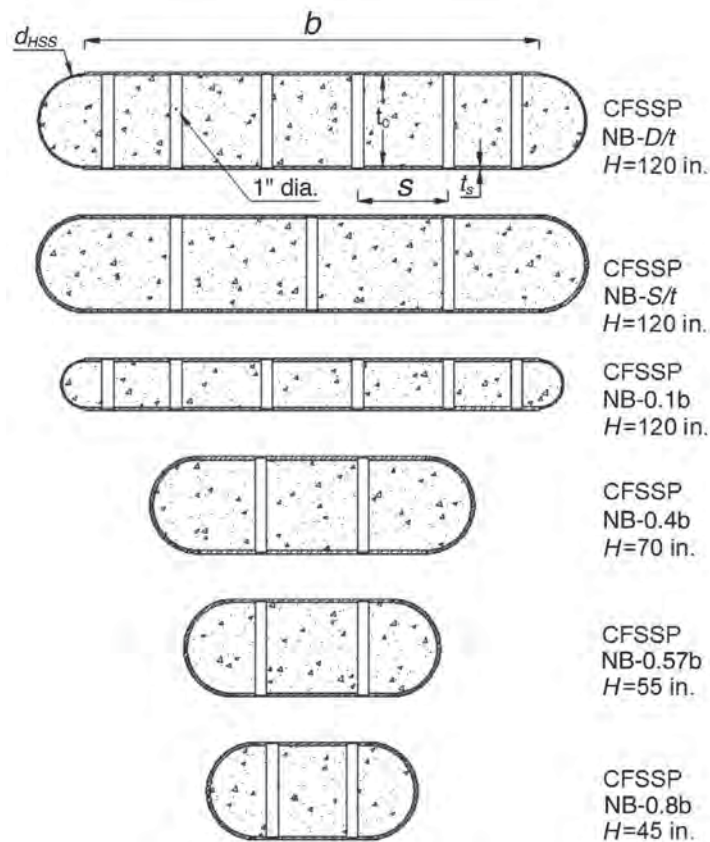
Fig. 8. Wall cross section used in the parametric study.

and concrete. Note that different Y-axes are used in Figure 9 to better show the hysteretic contributions of each parts of the wall and the comparison of total strength versus plastic flexural strength. The plastic flexural strength is shown in terms of base shear ($V_p = M_p/H$). As shown for all cases, the plastic flexural strength, calculated using simple plastic theory, was exceeded by the finite element model results.

Note that the steel material model does not have any damage properties; therefore, no strength degradation can be obtained from the numerical model due to steel plate fracture under low-cycle fatigue loading. One way to estimate low-cycle fatigue life of these walls is to use the cumulative plastic strain values at failure, obtained based on experimentally observed steel plate fracture location and drift

as described earlier. Therefore, to compare the low-cycle fatigue life of these walls, Figure 10 shows lateral load versus cumulative plastic strain histories of failure critical elements, which are typically located at the middle of the buckled wave formed at the wall boundaries. Based on Figure 10, model NB-S/t has the highest plastic strain accumulation at a given drift, which is attributed to the larger plate buckling amplitudes it develops compared to the other cross sections considered. Note that model NB-0.1b has a coarse mesh at the wall boundaries due to its small wall thickness, and its results may be correspondingly more approximate. In order to approximate the failure drift ratio for these walls, a cumulative plastic strain at fracture of 1.5 is assumed [a reasonable approximate value, based on the reported failure
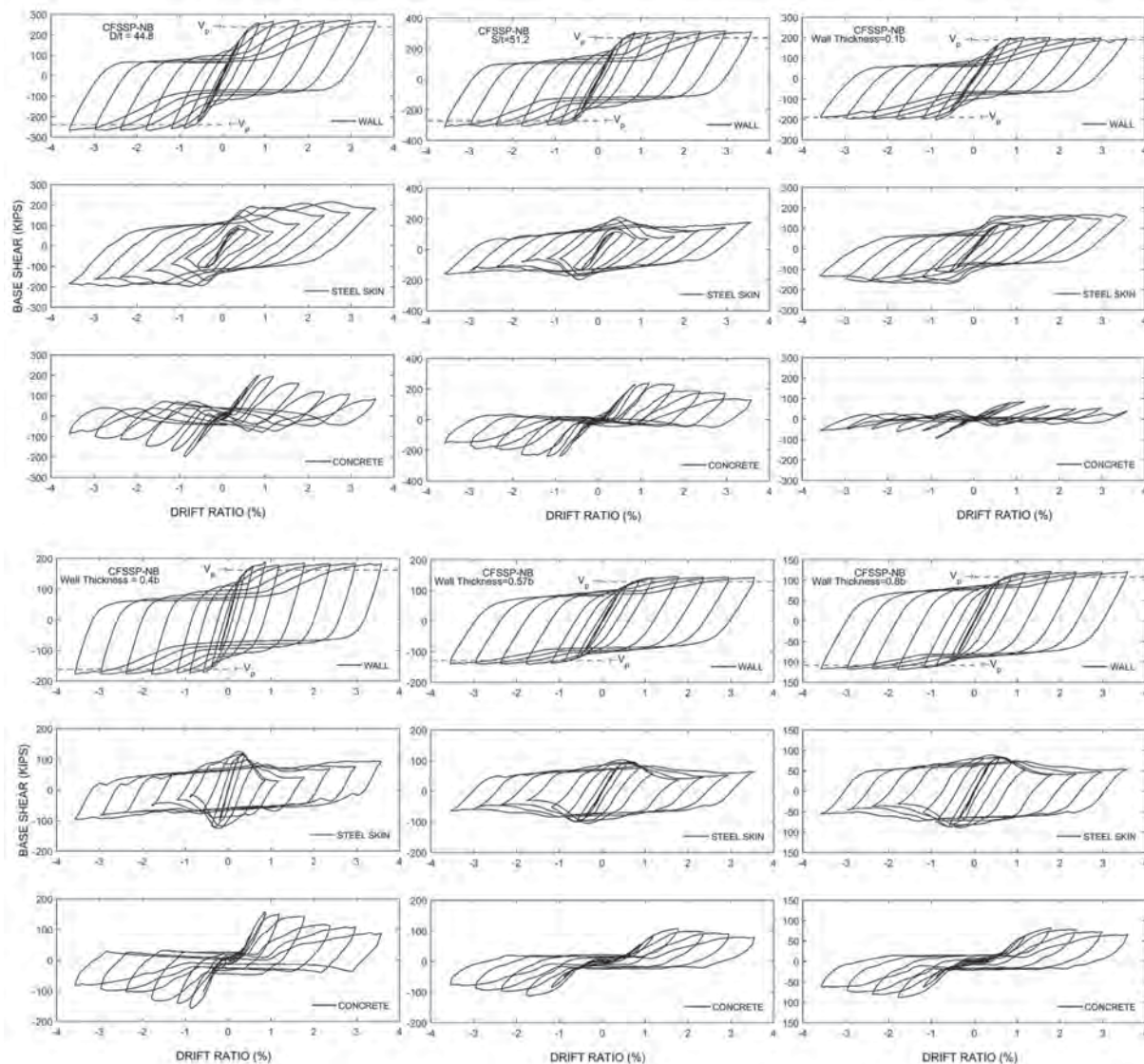

Fig. 9. Hysteresis loops of the of the walls with different cross sections.

cumulative plastic strain value of 1.40–1.45 obtained by Polat and Bruneau (2017) for the CFSSP-B2 wall model]. Based on this information, as shown in Figure 9, models NB D/t, S/t, 0.1b, and 0.4b could sustain their strength up to a 3% drift ratio, while models 0.57b and 0.8b could do so up to a 3.6% drift ratio.

T-SHAPED CFSSP-WALLS

The previously described finite element approach and techniques were then used to investigate the behavior of CFSSP-Walls having T-shaped cross sections. For this purpose, two different cross sections were considered: (1) a T-shaped wall tested by Eom et al. (2009), which was referred to as

DSCW3, and (2) an arbitrary cross section obtained by modifying the geometry of that DSCW3 wall. First, dimensions and properties of the materials used in those walls are presented. Then, to complement this, the plastic flexural strength of these walls are calculated using simple plastic theory and the same assumed uniform plastic stress distributions on steel and concrete sections used previously (Alzeni and Bruneau, 2014, 2017); closed-form equations are also provided for this purpose. Finally, experimentally reported lateral force versus drift and lateral force versus axial strain are compared with those obtained from the finite element analyses, and the numerical results are used to provide additional insights into behavior of T-shaped CFSSP-Walls.
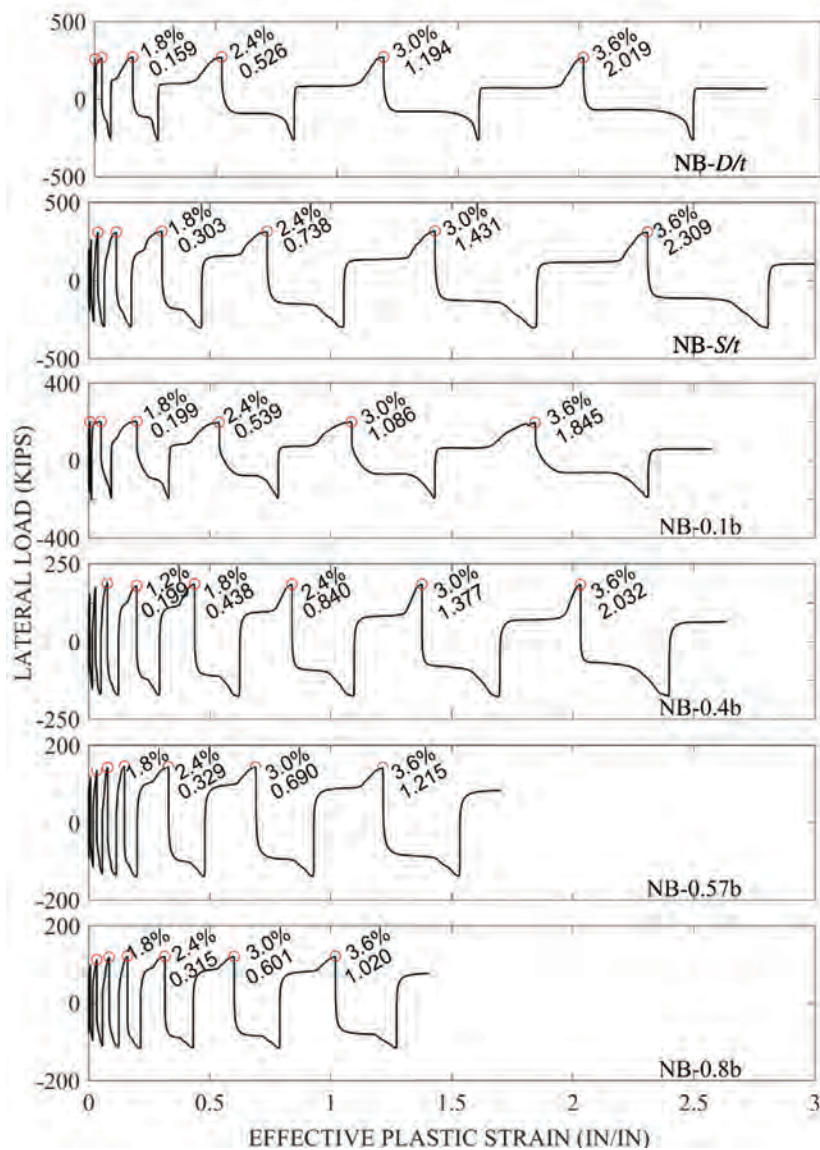

Fig. 10. Effective plastic strain histories of the fracture critical steel elements of the CFSSP-Walls.

Cross-Section Geometry, Material Properties, and Plastic Moment

Figure 11 illustrates the cross-section and dimensions of the DSCW3 wall, together with parameters used to develop closed-form equations to calculate plastic flexural strength under negative and positive drift. The DSCW3 section has a full depth, b, of 39.4 in. (1000 mm); a flange width, w, of 23.6 in. (600 mm); a uniform wall thickness (same for web and flange), t, of 4.7 in. (120 mm); a steel plate thickness, t_s, of 0.4 in. (10 mm); and a tie-bar spacing to steel plate thickness ratio, S/t_s, of 30. Figure 11 also illustrates the axial stress blocks for negative (Figure 7a) and positive (Figure 7b) wall drifts, and the corresponding tension and compression force vectors used to obtain the plastic neutral axis and plastic moment of the cross sections. Note that these two selected stress distributions assume that the plastic neutral axis is within the range 0 to $(b - t)$ for case a (negative drift) and within the range $(b - t)$ to $(b - t + t_s)$ for case b (positive drift). The closed-form equations for the plastic flexural strength [which assume uniform steel yield strength, F_y, and concrete compressive strength, f'_c] are derived subsequently. Table 5 presents the closed-form equations for C and M_p for these two cases, as well as all the other possible cases of plastic neutral axis locations, such as to cover any general cross-section dimensions (not illustrated). In Table 5 and Figure 11, C is the depth of the compression zone, which is calculated and derived from the axial force equilibrium in the cross section; other parameters are as defined previously. For the DSCW3 wall, the yield, F_y, and ultimate, F_u, strength of the steel plates are 55 ksi (383 MPa) and 79 ksi

(544 MPa), respectively, and the compressive strength, f'_c, of the filled concrete is 5.8 ksi (39.7 MPa).

Using the equations in Table 5, the geometry shown in Figure 11, and the material properties reported earlier, the plastic neutral axis of the DSCW3 wall was calculated to be located at 24.0 in. (610 mm) (Figure 11a) and 4.7 in. (119 mm) (Figure 11b) from the outermost compression fiber of the wall under negative and positive drift, respectively, which correspondingly falls in the wall's web and in the bottom steel plate of the wall flange, respectively. The base shear force at plastic moment, given as M_p/H, is 272 kips and 230 kips under negative and positive wall drifts, respectively.

Note that for some locations of the plastic neutral axis (for different geometries), greater axial strain values may develop in the wall web or wall flange, which in turn may affect the buckling behavior of the steel plates and change the ultimate wall strength. To address these issues that may arise, and to investigate the effect of wall geometry on wall behavior, another wall with different cross-section geometry was considered here. This additional example has a wall flange width equal to about three times that of the DSCW3 wall, but with the same wall web and material properties, and is referred as DSCW3-3W. Table 6 presents the plastic neutral axis and plastic moment values of both the DSCW3 and DSCW3-3W walls under negative and positive drifts. Note that for the DSCW3-3W wall, the plastic neutral axis is located within the thickness of the steel flange bottom plate under negative drift and within the thickness of the infill concrete of wall flange under positive drift.
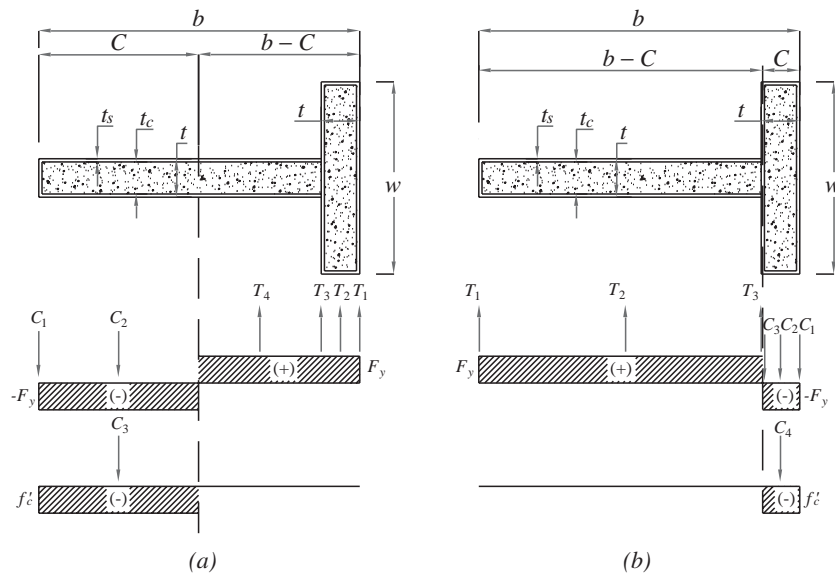

Fig. 11. Cross-sectional parameters of T-shaped walls and stress blocks used to calculate flexural strength of T-Walls: (a) T-Wall under negative drift; (b) T-Wall under positive drift.

Table 5. Plastic Flexural Strength of T-Walls	
Location of PNA	**Equations for M_p and C (positive drift)**
In flange concrete	$M_p = (0.5t_s^2 w - Ct_s w + 0.5C^2 w)f_c' + \left\{ -2t_s^3 + (w - 2.5t_c)t_s^2 + \left[2C^2 + (-t - 2b)C + wt_c + b(b + t_c) \right] t_s \right\} F_y$
	$C = \dfrac{t_s(2F_y b + F_y t_c + f_c' w)}{4F_y t_s + f_c' w}$
In bottom plate of flange	$M_p = (-0.5t_c^2 w + wt_c C - 1t_s wt_c)f_c'$ $\quad + \left\{ 8t_s^3 + (3.5t_c - 4b - 2C + 2w)t_s^2 + \left[(-1b + C + 3w)t_c + b^2 - 2wC \right] t_s + wt_c^2 + wC^2 - 2wt_c C \right\} F_y$
	$C = \dfrac{\left[-4t_s^2 + (2b + 2w - 3t_c)t_s + 2wt_c \right] F_y - t_c wf_c'}{2wF_y}$
	Equations for M_p and C (negative drift)
In wall web	$M_p = (-0.5t_c Ct_s + 0.5t_c C^2)f_c'$ $\quad + \left\{ 4t_s^3 + (-2w + 4C - 4b + 1.5t_c)t_s^2 + \left[2C^2 + (-2w + t_c - 2b)C + b^2 + 2wb - 1wt_c \right] t_s \right\} F_y$
	$C = \dfrac{t_s F_y (2b - t_c - 4t_s + 2w)}{4F_y t_s + f_c' t_c}$
In bottom plate of flange	$M_p = \left[4.5t_s^2 t_c + (-3bt_c + 3t_c^2)t_s + 0.5b^2 t_c - bt_c^2 + 0.5t_c^3 \right] f_c'$ $\quad + \left\{ 8t_s^3 + (2C + 2w + 3.5t_c - 6b)t_s^2 \left[(-C + 3w)t_c + (-2b + 2C)w + b^2 \right] t_s + t_c^2 w + (-2b + 2C)wt_c \right.$ $\quad \left. + (-2bC + C^2 + b^2)w \right\} F_y$
	$C = \dfrac{\left[(-2w + 3t_s)t_c + 4t_s^2 + (-2b - 2w)t_s + 2wb \right] F_y - t_c(b - 3t_s - t_c)f_c'}{2wF_y}$
PNA = plastic neutral axis C = depth of the compression zone M_p = plastic moment of the cross section	

Table 6. Plastic Neutral Axis and Plastic Moment Values of the T-Walls				
	DSCW3		**DSCW3-3W**	
Wall Parameters	**(–) Drift**	**(+) Drift**	**(–) Drift**	**(+) Drift**
C (in.)	24.0	4.71	35.0	4.0
M_p (kip-in.)	39936	33768	50932	40683
V_p (kips)	272	230	347	277

Finite Element Modeling of T-Shaped Walls

Finite element models of the DSCW3 and DSCW3-3W walls were developed using LS-Dyna following the same modeling approaches described previously. Material properties for steel and concrete were defined using the values given previously. For the bi-linear steel material model definition, the elastic modulus was 29,000 ksi (200,000 MPa), and the post-yield tangent modulus was 234 ksi (1610 MPa).

The DSCW3 cantilever wall tested by Eom et al. (2009), with a height of 142 in. (3600 mm), was fixed at its base by welding the steel skin of the wall to an ~2-in. (50-mm)-thick base plate, itself bolted to a concrete foundation. The specimen was strengthened at the bottom by using cover plates with a thickness of 0.40 in. (10 mm) over a height of 11 in. (280 mm). In the finite element analyses, the base plate used in the experimental set-up was not modeled; instead, the wall model was perfectly fixed at the base. The finite element

models followed the experimental loading protocol (which terminated at −2.0% drift ratio), but applying only one cycle per drift amplitude as opposed to two during the experiment. Note that initial failure of the tested DSCW3 wall occurred when the web wall failed from the local buckling of the steel plate, crushing of the infill concrete, and tie-bar fracture at −2.0% drift ratio that resulted in strength degradation of the wall (Eom et al., 2009). After this wall failure first occurred during a cycle in one direction [deemed the negative direction by Eom et al. (2009)], testing continued by monotonic loading of the wall in the opposite (positive) direction until tensile fracture of the steel plate occurred at a 4.9% drift ratio (Eom et al., 2009).

Figure 12 shows the LS-Dyna model for the DSCW3 wall. To expedite the run-time of the simulation, only half of the wall was modeled using symmetry boundary conditions, and the numerical solution was executed using the nonlinear static implicit solution procedure of the program. Figure 13 shows the cyclic displacement history and the user-defined step size employed in the definition of displacement curves

in the program. The step size curve adjusts the time steps of the displacement history protocol over the analysis period and is useful to expedite the numerical simulation in the elastic range (by using larger step size) and improve numerical convergence in the inelastic range of the wall simulation (by using smaller step size).

Simulation Results of T-Shaped Walls

Figure 14 shows the lateral load versus drift ratio relationship of the DSCW3 and DSCW3-3W wall models, including individual contributions from the steel skin and the infill concrete. The numerical model developed for the DSCW3 wall exhibited stiffer behavior than measured in the test, but no attempt was made here to calibrate the model's stiffness because it would have required explicit modeling of the base plate and the stiffness of the bolts used to attach the base plate to the floor (which was beyond the scope of the current work and not of interest). As shown in the figure, the base shear strength of the wall that corresponds to the calculated
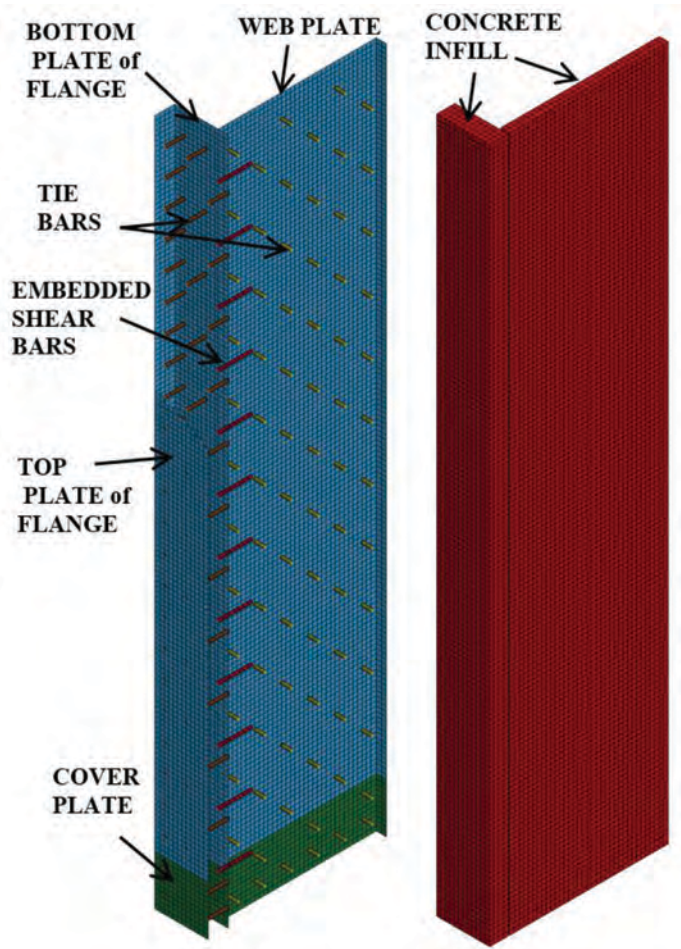

Fig. 12. LS-Dyna model of the half-symmetric T-Wall DSCW3.

plastic moment was exceeded, which indicates that the ultimate flexural capacity of the wall can be conservatively predicted by the simple plastic theory. For the DSCW3 model, the plastic moment was achieved at about +0.7% and −0.6% drift, whereas it was reached at +1.0% and −0.8% drift for the DSCW3-3W model. The ultimate moment capacity achieved by the finite element models (i.e., at ±2.0% drift) are greater than the calculated plastic moment capacity by a factor of 1.23 and 1.24 for the DSCW3 wall and 1.12 and 1.25 for the DSCW3-3W wall. The experimentally measured maximum strengths of the DSCW3 wall (in positive

and negative drift) are shown in Figure 14a, by $V_{u(EXPR)}$, to be 290 kips and 273 kips under positive and negative drift, respectively. The ultimate wall strength under the positive drift was successfully captured by the numerical model, whereas in the negative direction, the ultimate wall strength was overestimated by an amount of 23%. The finite element model was able to capture the local buckling of the wall's web steel plate at −2.0% drift ratio and subsequent concrete crushing, which is also indicated by the strength degradation in the negative displacement direction, shown in Figure 14.
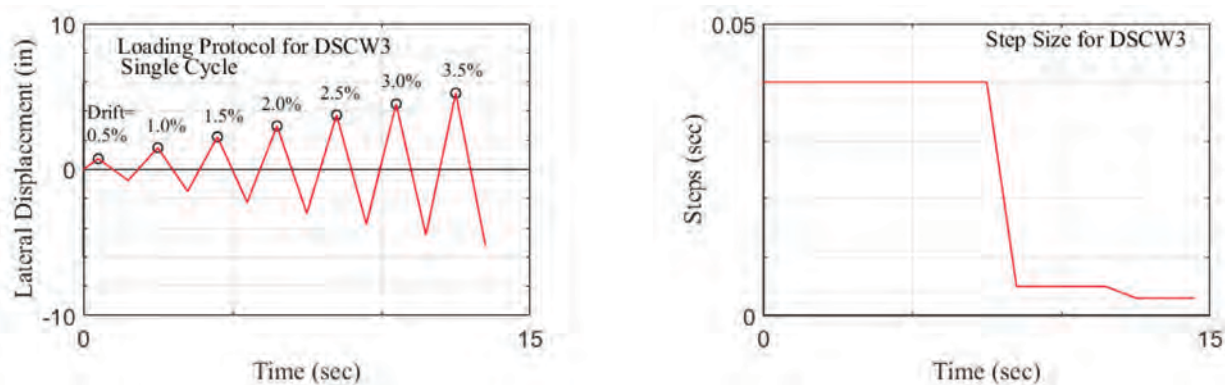

Fig. 13. Displacement loading history and time step size used in the finite element analyses of DSCW3 and DSCW-3W wall models.
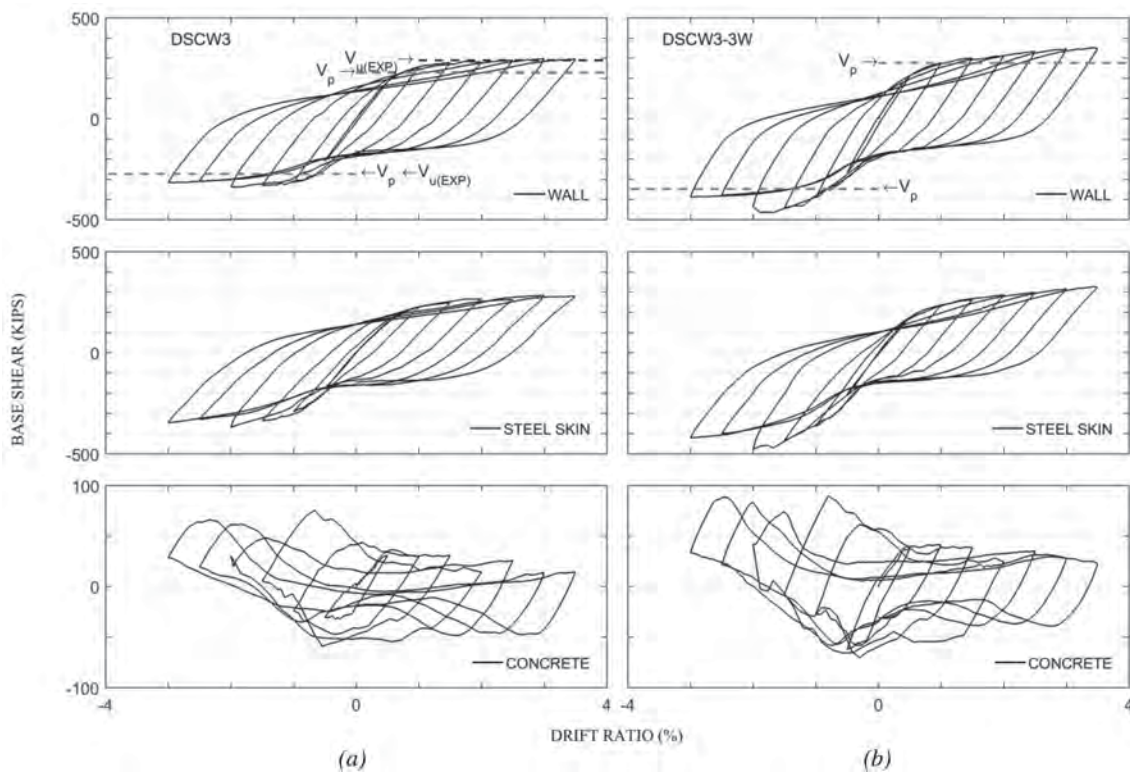

Fig. 14. Hysteresis curves of the LS-Dyna models of T-Walls: (a) DSCW3; (b) DSCW3-3W.

Note that the finite element simulation does not capture tie-bar fracture, which was one of the failure mechanisms of the Eom et al. (2009) specimen at a −2.0% drift ratio in addition to steel plate local buckling of web plate and concrete crushing. Simulation results of the DSCW3 model indicate that the bar located above the buckling wave (located at the outermost location of the first row of tie-bars above the cover plate) starts yielding at a 1.5% drift ratio. Because all the steel material model definitions (i.e., for steel plates and tie-bars) assumed bi-linear behavior with strain hardening, the possible strength degradation due to tie-bar fracture was not captured, which otherwise would have resulted in more severe strength degradation at −2.0% and beyond. Therefore, the wall response shown in Figure 14 is representative of the expected wall response if tie-bar failure can be prevented.

The axial strain values obtained from the finite element analyses results were found to be in agreement with those experimentally measured at the outermost wall depths and above the cover plates (i.e., at 12 in. from the base). Figure 15 shows the lateral force–axial strain histories obtained from the numerical model of DSCW3 model. The tensile axial strain at the end of the web wall, consistent with what was reported by Eom et al. (2009), was greater than that in the wall flange (attributed to the location of the neutral axis, which is close to the wall flange). The respective experimentally measured and finite element obtained axial strain values at the end of the wall web plate are 0.023 versus 0.026 at +1.0% drift and 0.041 versus 0.047 at +1.5% drift, and strain values for the steel plate at the wall flange are 0.021 versus 0.018 at −1.5% drift. Note that strains were obtained at regions away from the buckled zone of the plates to be

representative of plane–strain values and avoid the regions of strain magnification due to local buckling; also note that for the wall flange, readings at the outermost location on the Y-axis are used here. Moreover, the reported tensile strain at failure is 0.041 mm/mm, whereas the numerically obtained value is 0.047 mm/mm.

The following sections present finite element analysis results for cyclic stress-strain history of the steel plates at the wall base, initiation and progression of steel plate buckling of the web and flange steel plates of the T-shaped walls, and the shear and normal stress distribution of the steel and concrete parts of the walls under increased cyclic wall drifts.

Stress-Strain History of Steel Plates in DSCW3 and DSCW3-3W

One of the purposes of analyzing wall DSCW3-3W (a modified geometry of DSCW3) was to investigate how behavior is affected by different neutral axis locations, which may increase or decrease axial strain and stress demands and affect the onset of steel plate buckling and ultimate wall strength. As shown in Table 6, changing the geometry from DSCW3 to DSCW3-3W reduces the compression depth under positive drift, increases it under negative drift, and modifies the force vectors (shown in Figure 11) used to calculate the plastic flexural strength of the section. Note that for DSCW3-3W under positive drift, the neutral axis is located within the thickness of the infill concrete of the wall flange.

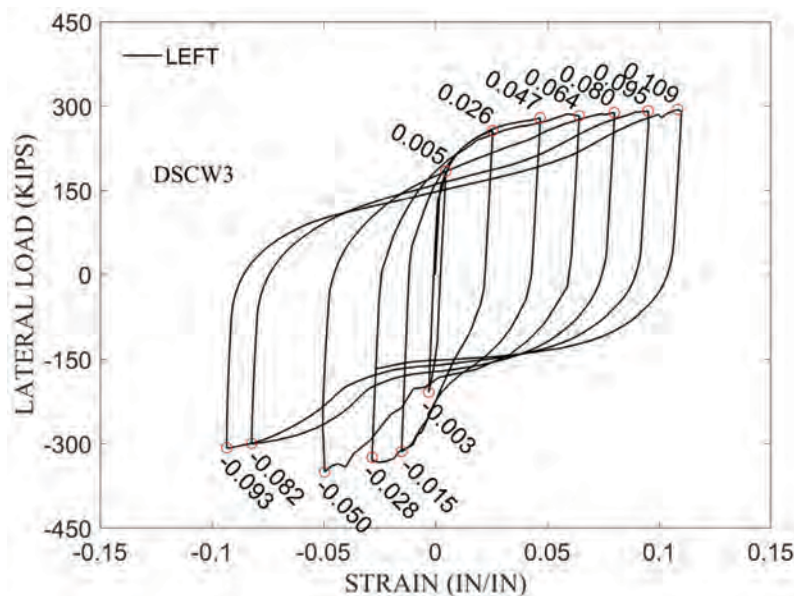Shell elements located just above the cover plate (at a 12-in. distance from the wall base) and evenly distributed

Fig. 15. Lateral load versus steel strain relationship obtained from the LS-Dyna model for DSCW3.

along the cross-sections of the models were used to plot vertical uniaxial stress-strain response of these elements under cyclic loading. Figure 16 shows the location of these selected elements on the half-symmetric cross section of the finite element models and the global coordinates used. Figures 17 and 18 show the vertical uniaxial stress-strain history of the selected shell elements shown in Figure 16 (the shell middle integration point values are plotted). Note that the X-axis is not the same in all plots in these figures to better show the various points in each plot. The points when peak positive drift amplitudes were reached are marked on each curve using numbers from 1 to 6, respectively corresponding to the first and sixth drift amplitude level (+0.5% and +3.5% drift ratio, respectively). Plastic neutral axis locations of the wall models can also be bracketed by observing the sign of the axial stresses in Figure 17 (defined as positive in tension) at each specific peak positive drift amplitudes; for example, from Figure 17a, it is seen to be within the range of 25.2 to

34.1 in. in the global X-axis direction (defined in Figure 12) for the DSCW3 wall model.

Figure 17 also shows that the stress-strain response of the web plate is approximately similar for both models except in regions close to wall plastic neutral axis. For both models, yielding of the wall web plate starts at about 0.5% drift at the outermost location.

Figure 18 shows that yielding in the wall flange steel top plate of the DSCW3 model initiates at about +1.0% drift and at about +2.0% drift for the DSCW3-3W model. On the other hand, yielding of the bottom plate of the DSCW3 model initiates at about +2.0% drift, whereas yielding never occurs for the bottom plate of the DSCW3-3W model. Moreover, the bottom plate of the DSCW3-3W model is in tension under peak positive drift, which indicates that the neutral axis is located somewhere between the bottom and top plates but close to the bottom plate. The stress-strain response of both the top and bottom steel plates of the wall flange of the
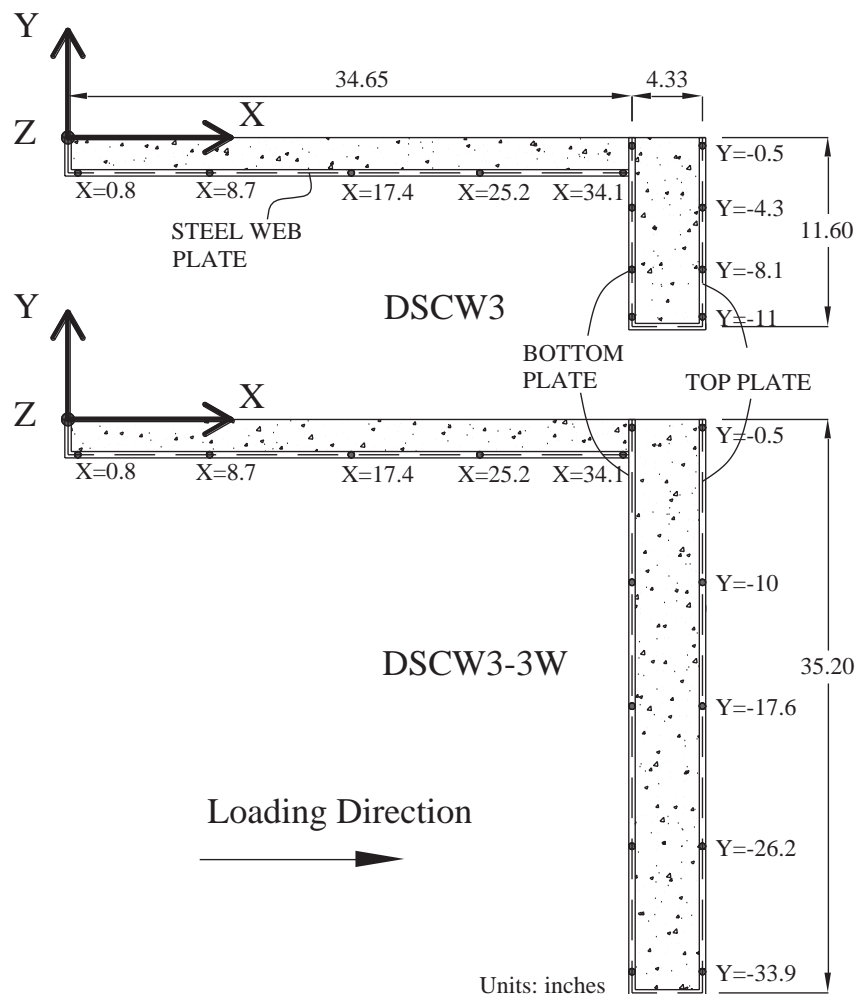

Fig. 16. Half-symmetric cross section of the DSCW3 and DSCW3-3W wall model and selected steel element location in the global coordinate system.
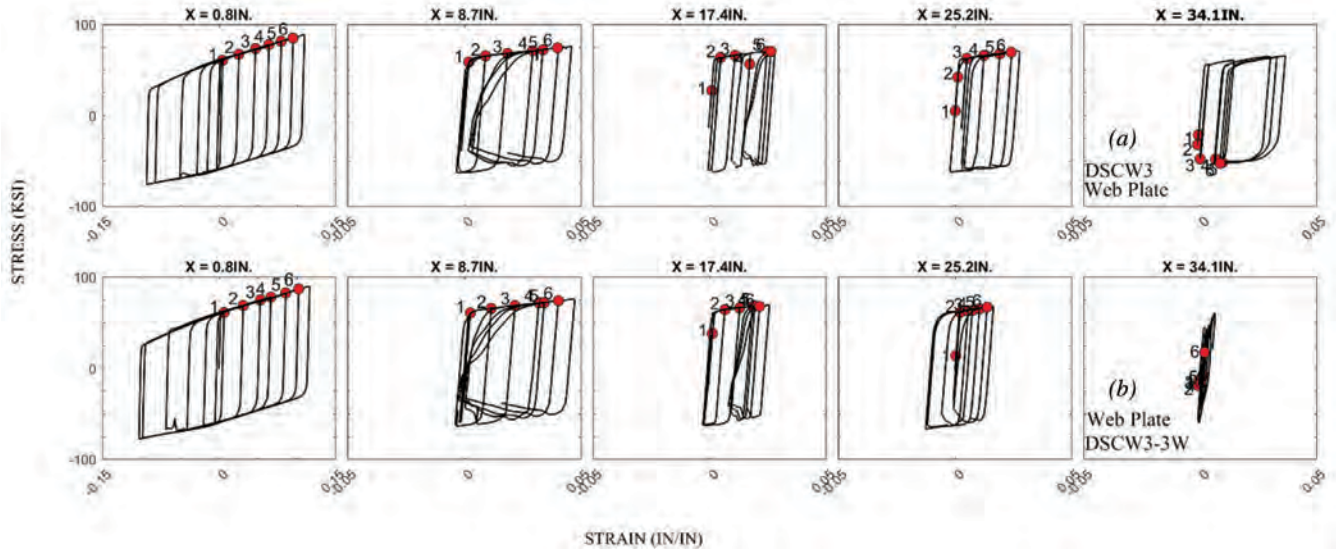
Fig. 17. Stress-strain relationship of steel web plate at 12-in. height: (a) DSCW3; (b) DSCW3-3W.
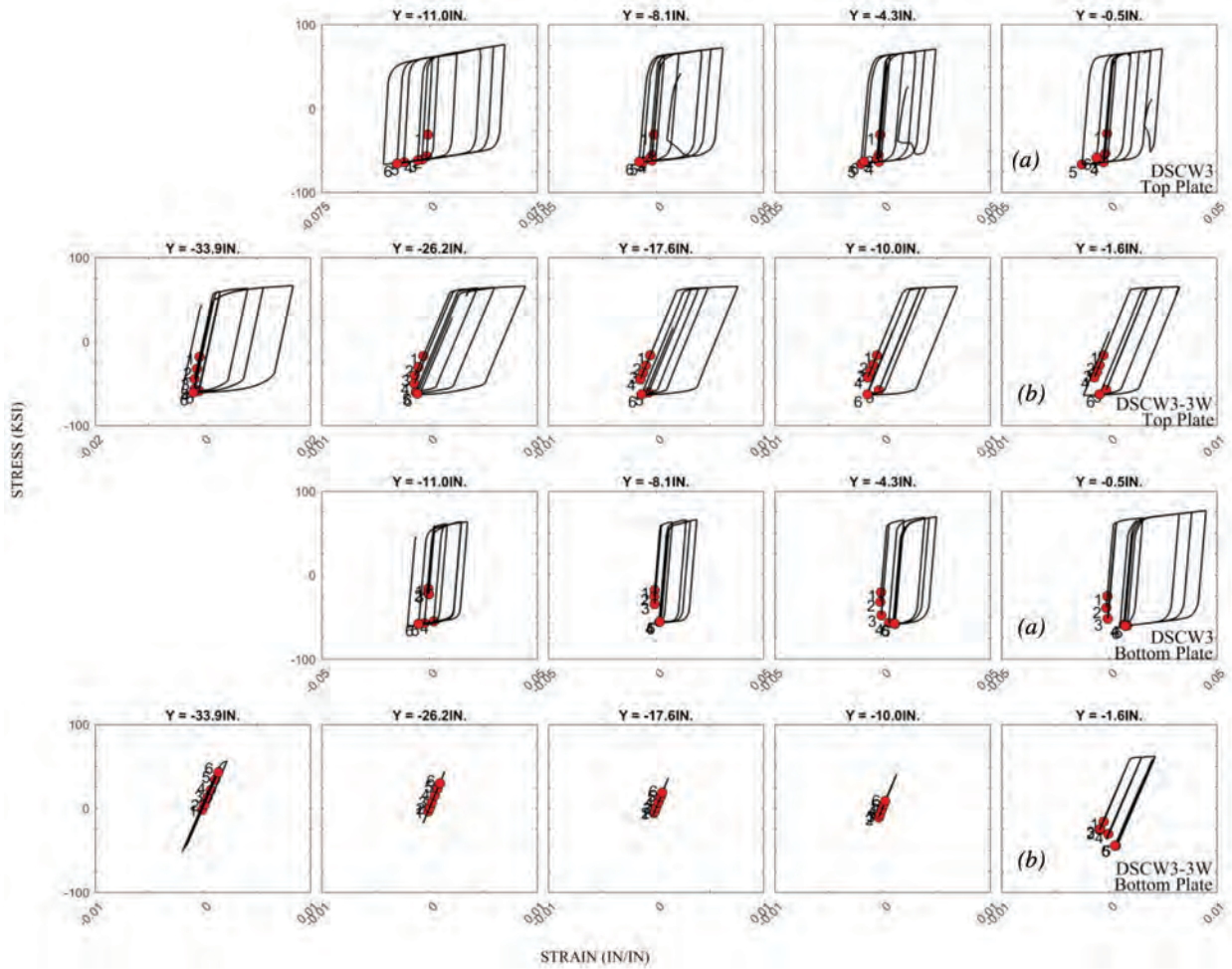

Fig. 18. Stress-strain relationship of steel flange top plate at 12-in. height: (a) DSCW3; (b) DSCW3-3W.

DSCW3-3W model at a 24-in. wall height (one tie spacing above the location considered in Figure 18) indicates total elastic response for all drift considered (not shown here).

Figure 18 reveals that shell elements located closer to the mid-flange width (closer to wall centerline) at this wall elevation (12 in.) attains lower vertical strain values than the ones located further away. This behavior (more significant for the DSCW3 wall model) was deemed to be a consequence of the flange top plate buckling pattern, which exhibited higher amplitude buckling waves toward the wall centerline (buckling wave amplitudes are presented in the following section). These higher strain values at the outermost elements are also a result of increased strain demands in this region due to the formation of compression diagonals following the plate buckling (not shown here but typically visible when plotting principal stress vectors). However, stress-strain histories obtained at higher wall elevations (i.e., at 24 in., where local steel plate buckling does not develop) than considered in Figure 18 show that the vertical strains are higher close to wall centerline.

Steel Plate Local Buckling

Experimental studies of CFSSP-Walls (Alzeni and Bruneau, 2014, 2017; Eom et al., 2009) showed that steel plate buckling eventually develops during their cyclic flexural response. Studying the individual strength contribution of these walls using the finite element methods (presented previously) revealed that steel plate buckling may or may not affect the global wall strength; however, it may modify the contributions of the individual wall parts to the total strength. As described earlier for the CFSSP-Walls tested by Alzeni and Bruneau (2014, 2017), steel plate buckling reduces the contribution of the steel plates to total strength, but the wall strength is not proportionally reduced because the force demand partially shifts to the concrete infill. However, for the T-shaped CFSSP-Wall tested by Eom et al. (2009), the concrete infill could not sustain the force demand itself following the steel plate buckling, which resulted in an early failure of the wall.

For both the DSCW3 and DSCW3-3W wall models, local buckling of the steel plates developed between the second and the third row of tie-bars, whereas buckling developed between the third and the fourth row of tie-bars in the actual DSCW3 specimen. Figure 19 shows the buckling wave amplitudes of the steel web plates (Figure 19a) and steel flange top plates (Figure 19b) of the DSCW3 and DSCW3-3W models along their horizontal lengths against increasing peak drift amplitudes (web plate buckling is shown under negative drift, whereas steel flange plate buckling is shown under positive drift). Note that for the DSCW3-3W model, steel flange plate buckling was not significant and is not shown in Figure 19b. The figure shows that for both models, web plate local buckling develops at −1.0% drift

and gradually increases in amplitude under larger drifts. The tensile axial strain (obtained from the outermost steel element of the web wall) at the onset of local buckling of the DSCW3 model ($S/t_s = 30$) is 0.026 in./in. (see Figure 15). This value is comparable to those obtained for the fixed-base CFSSP-Walls analyzed previously [i.e., 0.024 in./in. for CFSSP-NB1 ($S/t_s = 25.6$), seen in Figure 3]. Figure 19 shows that web plate buckling wave amplitudes are larger for the DSCW3-3W model than the DSCW3 model at any given drift. This is mainly due to the larger compression depth of the cross-section of the DSCW3-3W model (thus larger axial strains) than the DSCW3 model under negative drift.

Stress Analysis of Steel Skin and Infill Concrete of T-Shaped Walls

The previously developed simplified solutions to predict the wall neutral axis and plastic flexural strength of the T-shaped CFSSP-Walls assumed that uniform uniaxial yield strength of the steel skin and uniaxial compression strength of the concrete infill was attained on each side of the plastic neutral axis of the cross section of the wall. Although this approach is simple and practical to conservatively predict the ultimate wall strength, the actual stress distribution may vary due to steel plate buckling, stress amplitudes and distribution in the concrete compression zone, and von Mises interaction of stresses [for the planar CFSSP-Walls, hoop stresses increased the steel yield strength 15% on one side with vertical tensile stresses and reduced by the same amount on the other side of the wall's neutral axis with vertical compressive stresses, as shown by Polat and Bruneau (2017)]. Strain hardening of the steel skin (if steel plate buckling is avoided under high strains) may also have a noticeable effect for a T-shape wall that has a compression depth that varies significantly under different direction of wall drift as a consequence of the cross section being unsymmetrical. For planar CFSSP-Walls, Polat and Bruneau (2017) showed that assumption in the shape and amplitude of the concrete stresses has a major effect on the wall neutral axis location.

Finite element results were used to get shell (for steel sections) and solid (for concrete sections) element stress values to obtain stress distribution along the section depth at the prescribed wall elevation. These stress distributions, plotted for steel skin and concrete infill separately, are used also to quantify the normal and shear stress contributions on the steel plate yielding, the effect of confinement on the axial strength of the infill concrete.

The stresses are reported in the global coordinate system, such that assuming that in-plane loading lies in the X-Z plane, the vertical normal stress is given by σ_z, transverse normal stress is given by σ_x, and the shear stress is given by σ_{zx}. The origin of the global axes is as shown in Figure 16. Note that, the reported values of stresses in the concrete are actually an average of the through thickness solid elements.

Figures 20 and 21 show the stress distribution of the DSCW3 model, and Figures 22 and 23 show the stress distribution of the DSCW3-3W model at peak drift amplitudes along the depth of the cross sections of the walls (including flange depth). In these figures, shell element results are reported in panel a of each figure, and solid element results are reported in panel b of each figure. Note that, the wall depth (X-axis label of the figures) includes both the depth of the web and the thickness of the wall flange, The stress distributions of the steel skin were obtained from the web plate and flange side boundary plate that lie on the X-axis (see Figure 16). Also note that the stress distribution plots of the solid (concrete) elements (panel b of each figure) is discontinuous near the edge to denote that the infill flange and web concrete are physically separated (a steel plate is present in between the two, as shown in Figure 16).

The vertical stress (σ_z) distribution of the cross section reveals the location of the elastic and plastic neutral axis of the wall. For example, focusing on the results of the DSCW3 wall model shown in Figures 20 and 21, location of the plastic neutral axis falls into the wall web for both drift directions. For comparison with the theoretical prediction, for example, Figure 21 indicates a plastic neutral axis located at 9 in. under +3.0% drift, whereas theory predicted 4.7 in. (see Table 6). While, in this figure, the average concrete distribution and its strength is similar to that used in the simple plastic theory (i.e., uniform and $f_c' \sim 5.8$ ksi), the higher compression depth value obtained from the finite element analysis was deemed to be a result of wall flange top plate buckling. Similarly, the predicted compression depth was 24 in. under negative wall drift, which compares reasonably with the value indicated in Figure 20 (i.e., at −1.50% drift,
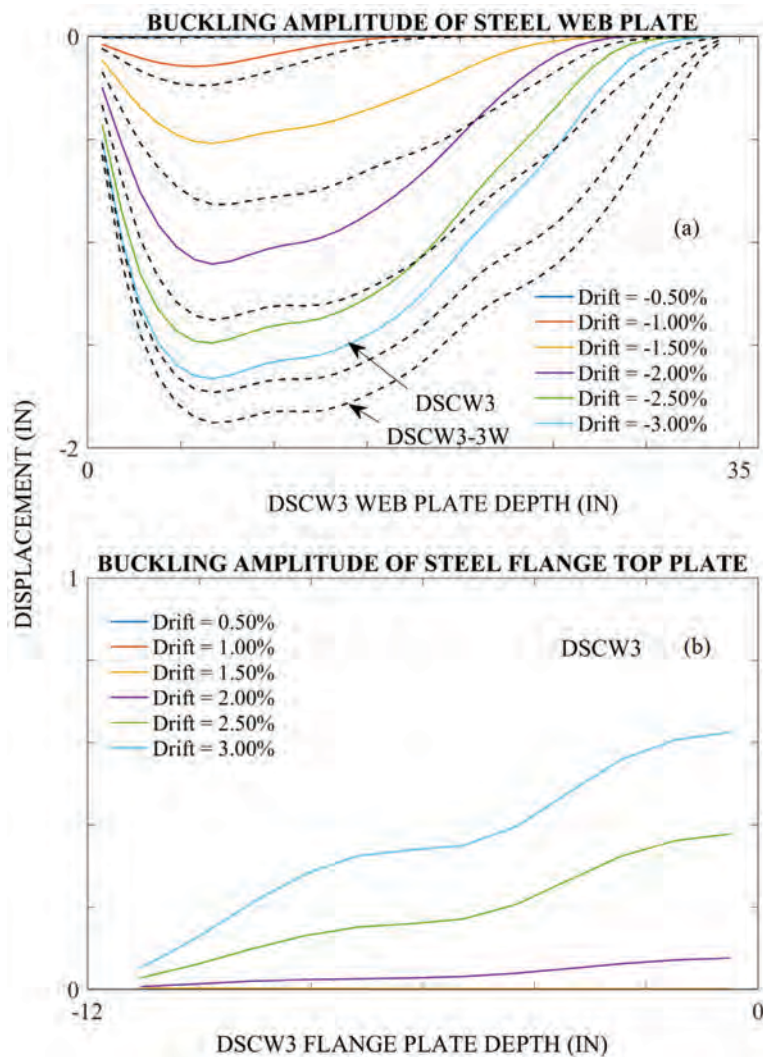

Fig. 19. Maximum local buckling amplitude of the LS-Dyna models of the T-Walls:
(a) steel web plate under peak positive drift; (b) steel flange top plate under peak negative drift.
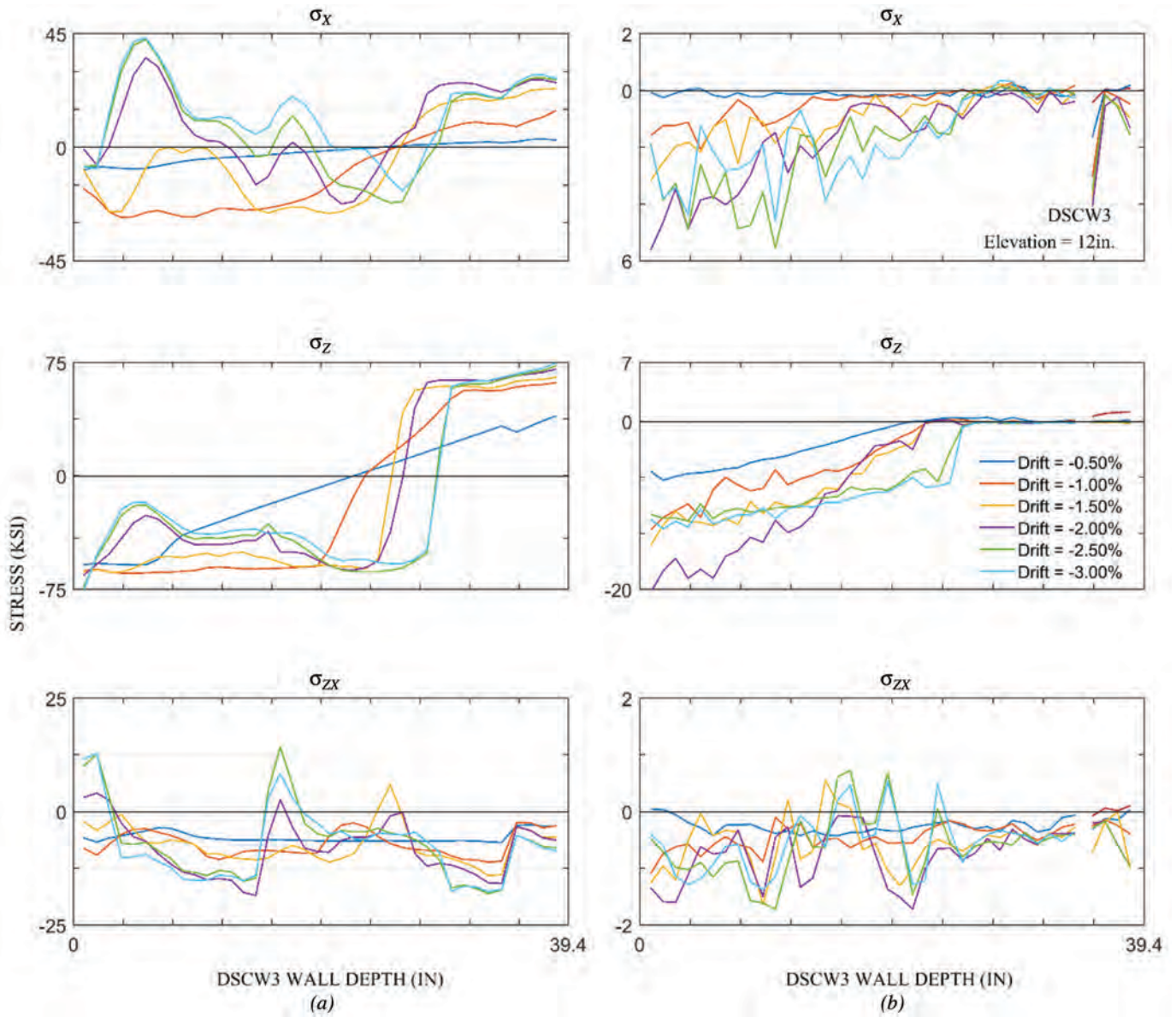
Fig. 20. Plane stress distribution of the cross section of the LS-Dyna model of DSCW3 located at 12-in. wall height under negative drift: (a) shell stress distribution in steel skin; (b) average solid stress distribution in concrete.
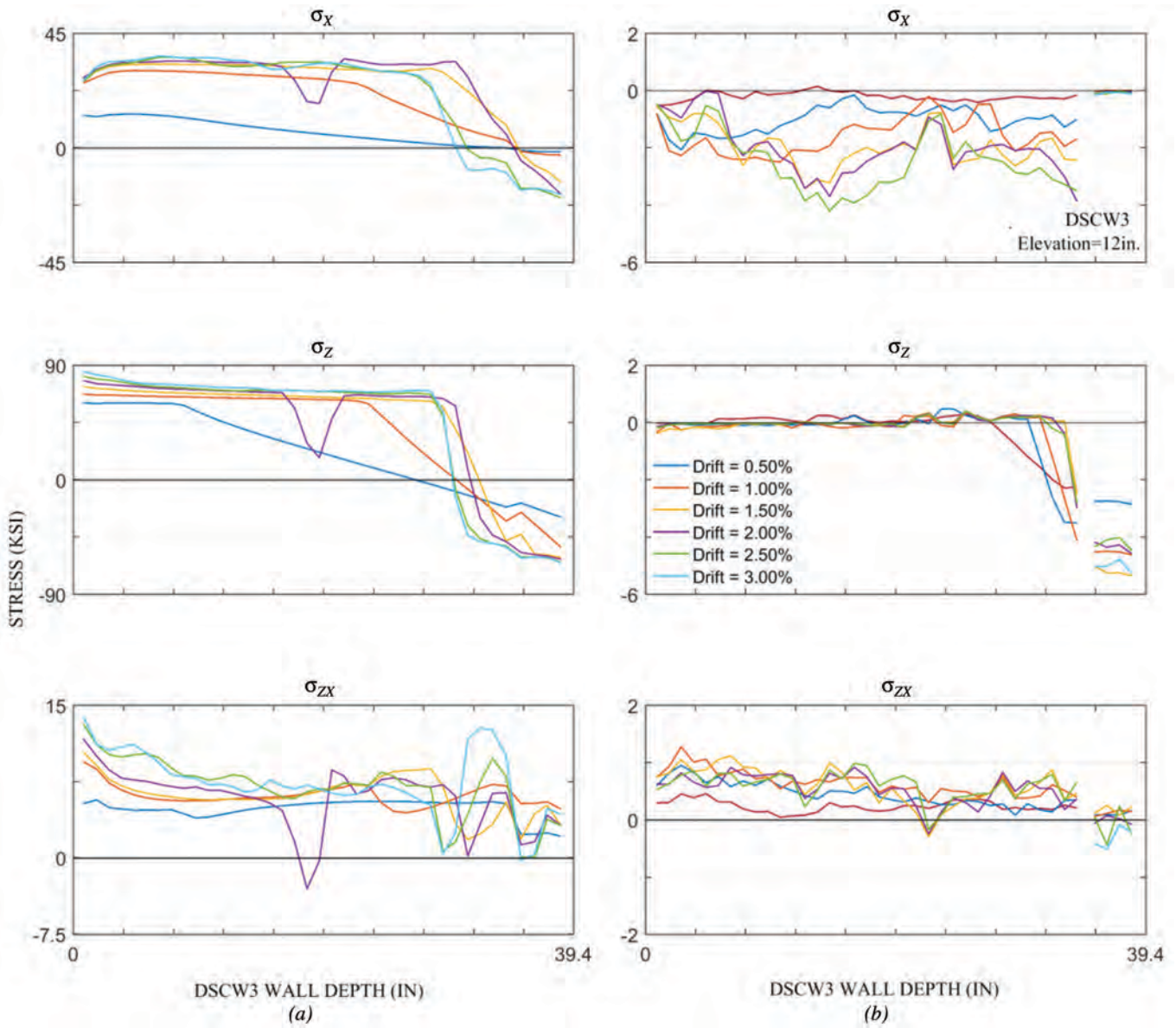
Fig. 21. Plane stress distribution of the cross section of the LS-Dyna model of DSCW3 located at 12-in. wall height under positive drift: (a) shell stress distribution in steel skin; (b) average solid stress distribution in concrete.
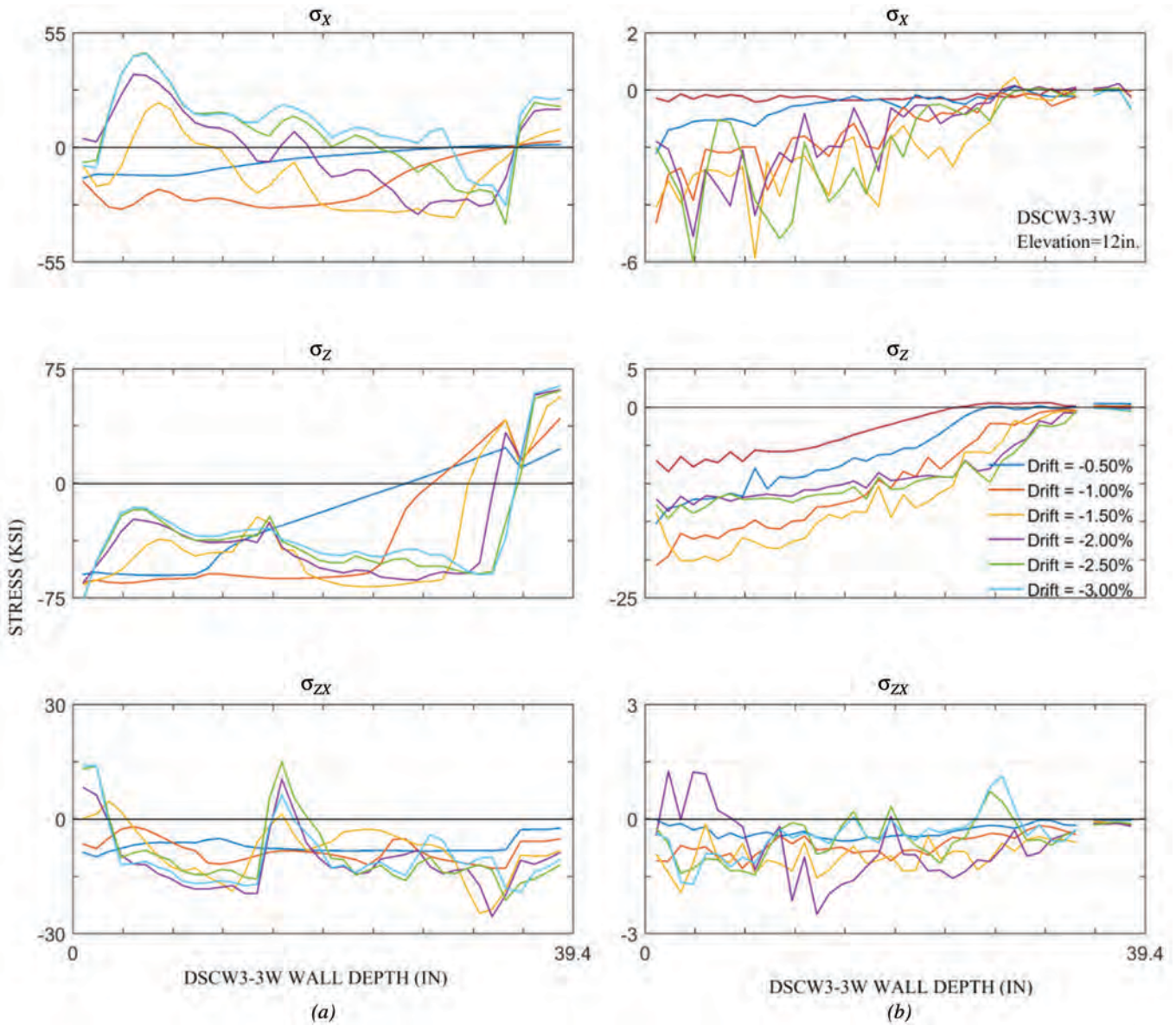
Fig. 22. Plane stress distribution of the cross section of the LS-Dyna model of DSCW3-3W located at 12-in. wall height under positive drift: (a) shell stress distribution in steel skin; (b) average solid stress distribution in concrete.
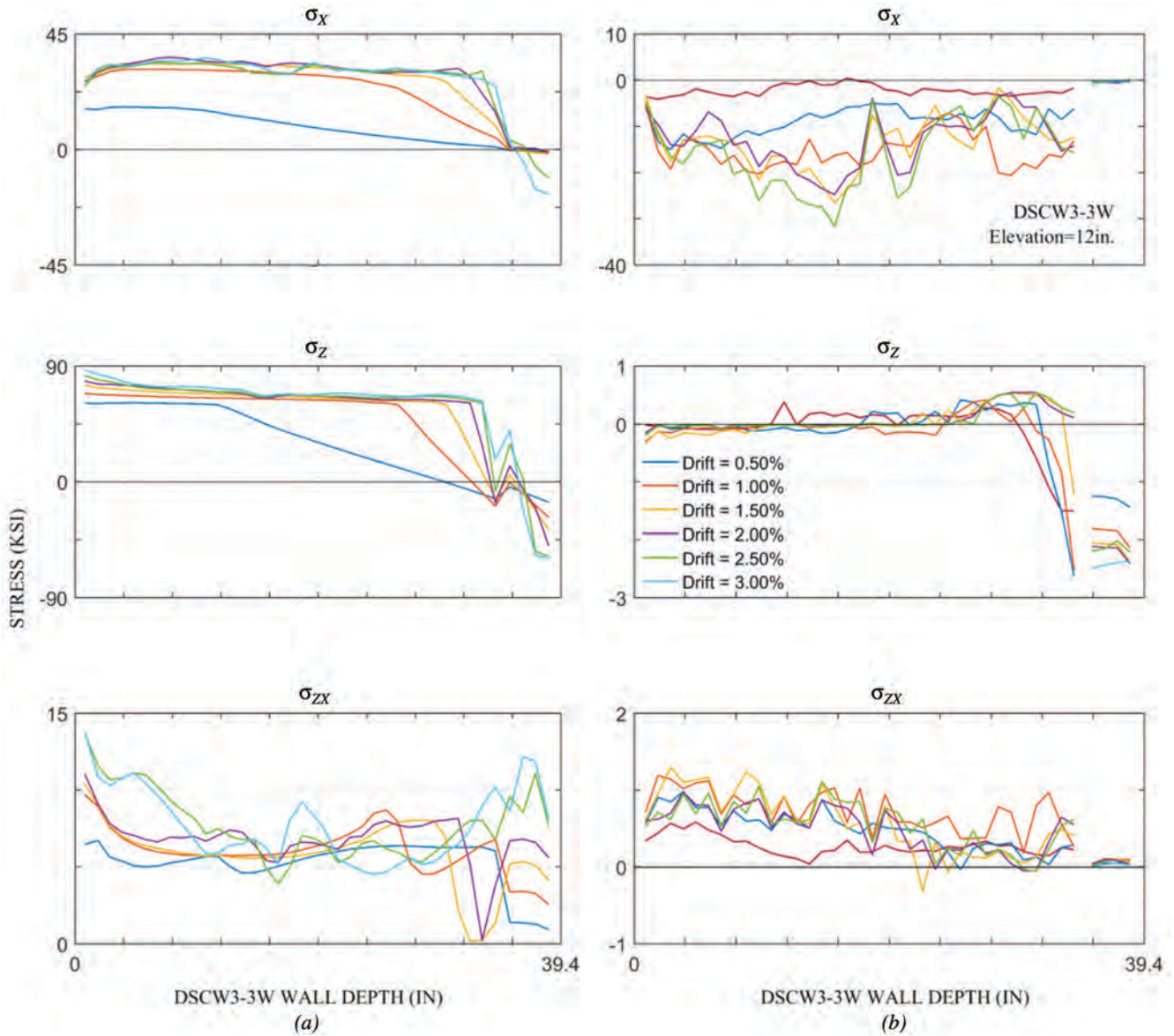
Fig. 23. Plane stress distribution of the cross section of the LS-Dyna model of DSCW3-3W located at 12-in. wall height under negative drift: (a) shell stress distribution in steel skin; (b) average solid stress distribution in concrete.

before severe web plate buckling developed). Note that, although the stress blocks are not perfectly consistent with the ones assumed in this case (i.e., the concrete compression stress distribution is more triangular than rectangular in Figure 20 at −1.50% drift), the increase of concrete compressive strength under confinement (up to 12 ksi compared to the unconfined strength of 5.8 ksi) is the reason for the close match between the compression depth values obtained from simple plastic theory and finite element results that exhibits nonuniform concrete compression distribution.

Steel and average concrete vertical stress distribution under negative drift shown in Figures 20 (DSCW3) and 22 (DSCW3-3W) indicate that concrete crushing follows steel plate buckling. For example, in these figures, steel strength starts to decrease following the steel plate buckling developed at −1.0% drift and is substantially reduced by −2.0% drift to the point where, at −2.0% drift, concrete compressive stresses have increased up to four times the uniaxial compressive strength. However, at larger drifts beyond −2.0%, concrete strength drops significantly as an indication of concrete crushing.

The average concrete vertical stress distribution of DSCW3 under positive drift (Figure 21) shows that infill concrete of the wall flange was able to reach its uniaxial compressive strength of 5.8 ksi, whereas for the DSCW3-3W model, it reached only half of its strength (Figure 23). The confinement effect of the steel web plate on the concrete is more notable under negative drift, as the results indicate in Figures 20 and 22. Average concrete vertical stress results, in these figures, indicate that concrete can attain strength values up to 20 ksi before the development of steel plate buckling, which is four times its uniaxial capacity. This is possibly an artifact of the computer model and would need to be challenged experimentally.

Under positive drift (i.e., with outermost element of wall web under tensile stresses), the transverse normal stresses of the wall web plate attain values as high as half that of the axial stresses, while the steel shear stresses attain values one-tenth of that.

Yielding and Prediction of Failure Drift Ratio of DSCW3

Polat and Bruneau (2017) established the cumulative strain value at fracture due to low-cycle fatigue upon repeated inelastic cycles for the CFSSP-B2 wall previously tested by Alzeni and Bruneau (2014). Assuming this value to be representative for composite walls of this type, the drift at which wall DSCW3 would have fractured can be estimated using the finite element model presented earlier. The DSCW3 T-shaped wall considered here was tested cyclically until buckling at −2% drift and monotonically after that up to fracture at 4.9% drift. Because the tensile strain at fracture for monotonically loaded steel differs from that obtained

from a cyclic low-cycle fatigue test, the finite element model is used to estimate failure drift of the DSCW3 wall had it been tested continuously under cyclic loading. This analysis follows the same procedure described earlier in the paper for planar fixed-base CFSSP-Walls.

Figure 24 shows the bottom third of the T-shaped walls subjected to the most damage (i.e., steel plate local buckling, higher von Mises yield stress, and effective plastic strain), under cyclic loading, at 3% drift (assuming the original cyclic protocol had been followed up to that drift, but only with a single cycle at each peak drift value). Note that the higher effective plastic region is where, during the test, fracture occurred under monotonic loading in the positive direction (following the cyclic loading terminated at −2.0% drift). Cumulative plastic strain history obtained from the element having the most severe effective strain (indicated by the effective plastic strain contours) was used to predict the failure drift ratio of the fixed base DSCW3 wall model had it been tested cyclically per the original protocol up to failure.

Figure 25 shows the history of the effective plastic strain of that element from the finite element simulation of the DSCW3 wall. The figure illustrates the logarithmic increase of the effective plastic strain under increased drift amplitudes of the wall. Table 7 presents the effective plastic strain values at peak drift amplitudes corresponding to the preceding protocol, as well as the values corrected to correspond to two cycles per drift at all drift levels [i.e., the originally intended Eom et al. (2009) protocol]. The corrected values indicate that this specimen would have sustained a ductility up to a drift of −3.0% (i.e., when it reached a cumulative plastic strain of 2.8) had the experiment continued under cyclic displacement. The dashed red line on that figure provides the same results if the specimen was subjected to monotonic loading after −2.0% drift. Note that the effective plastic strain values do not increase significantly after the +2.5 drift ratio in that case.

VERTICAL SHEAR FORCES OF THE WALL FLANGE TIE BARS

Finite element results of the DSCW3 and DSCW3-3W were used to obtain the shear forces on the tie-bars, to compare results between the two walls, and to investigate the relative contribution of the tie-bars in resisting shear for the two different T-wall flange depth considered. For demonstration purposes, tie-bars located at the third row from the wall bottom [located just above the cover plate in Eom et al.'s (2009) specimen] were used. This row has four tie-bars located 14.7 in. from the wall base in the DSCW3 model. Note that the half-symmetric finite element model has two tie-bars located at −4.8 in. and −9.5 in. on the global Y-axis from the symmetry plane of the wall, as shown in Figure 26. For the DSCW3-3W model, there are four bars in the
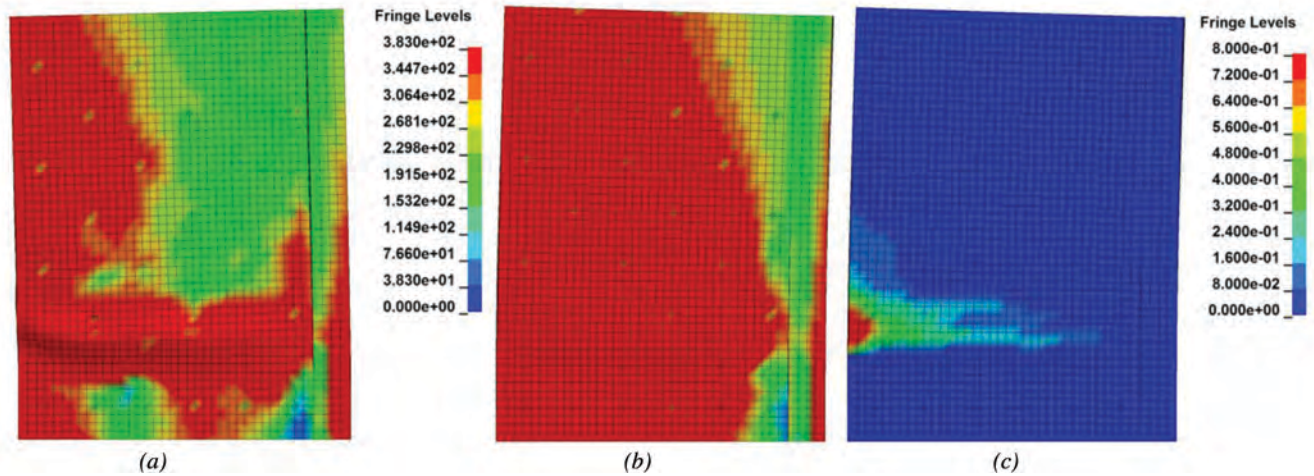
DSCW3
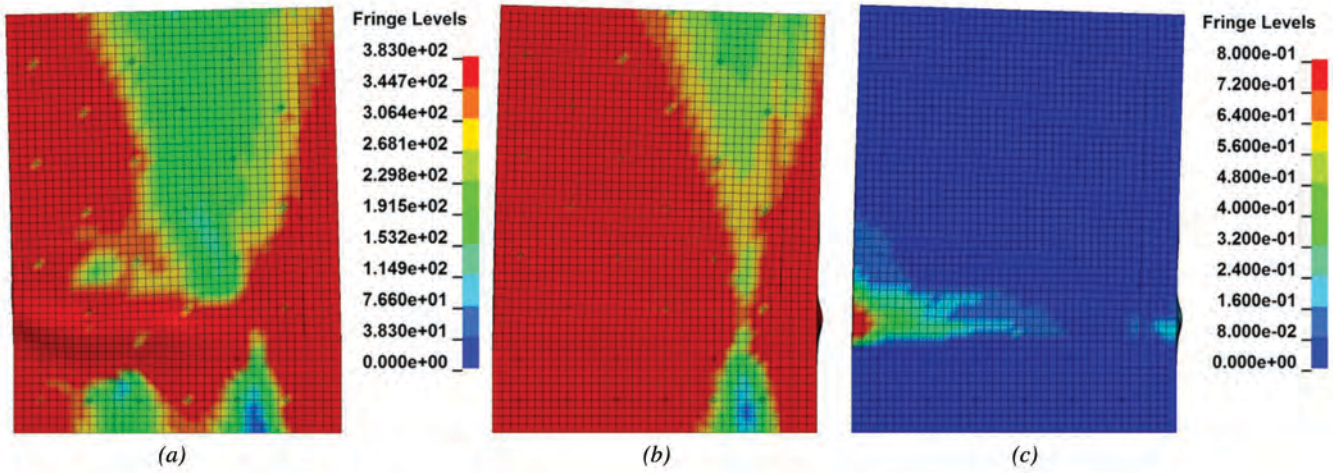
DSCW3-3W

Fig. 24. Stress and strain contours of the LS-Dyna model for DSCW3 (above) and DSCW3-3W (below): (a) von Mises stress at −3.0% drift; (b) von Mises stress at 3.0% drift; (c) effective plastic strain at 3.0% drift. (Note: Units shown are MPa; 1 MPa = 0.145 ksi.)

| Table 7. Effective Plastic Strain Values for the DSCW3 Wall Model at Peak Drift Amplitudes						
DSCW3						
Drift Ratio (%)	Cycle Order (i)	Cycle for Each Drift (n)	Plastic Strain (PS) LS-Dyna (single cycle)	$PS_{i+1} - PS_i$	$n \times PS_{i+1} - PS_i$	$\sum n \times (PS_{i+1} - PS_i)$ (corrected PS, double cycle)
0.5	1	2	0.003	0	0	0
−0.5	1	2	0.008	0.005	0.01	0.01
1.0	2	2	0.027	0.019	0.038	0.048
−1.0	2	2	0.067	0.04	0.08	0.128
1.5	3	2	0.124	0.057	0.114	0.242
−1.5	3	2	0.211	0.087	0.174	0.416
2.0	4	2	0.32	0.109	0.218	0.634
−2.0*	4	2	0.468	0.148	0.296	0.93
2.5	5	2	0.637	0.169	0.338	1.268
−2.5	5	2	0.87	0.233	0.466	1.734
3.0	6	2	1.117	0.247	0.494	2.228
−3.0	6	2	1.393	0.276	0.552	**2.78**
3.5	7	2	1.681	0.288	0.576	3.356
* Cyclic loading stopped in actual test due to web plate buckling and concrete crushing.						
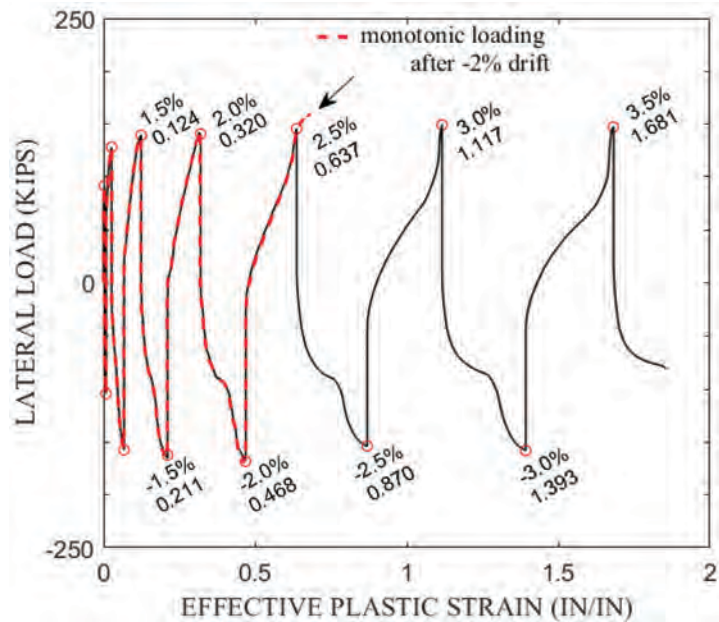
Fig. 25. *Effective plastic strain history of the fracture critical element of the web steel plate.*

half-symmetric finite element model in each row (eight bars in the actual wall), and they are located at −4.8, −14.3, −23.8 and −32.3 in. on the Y-axis from the axis of symmetry of the finite element model. as shown in Figure 26. Note that the tie-bars were modeled with beam elements that were located through the thickness of the infill concrete, and the end nodes of the beams were coupled with the solid nodes of the infill concrete. Figure 20 shows the history of the vertical shear forces at peak drift amplitudes of the wall models. The shear forces were reported at the centroid of each beam element (shown by the solid circles in the figure). Results indicate that interior and exterior beam elements are subjected to opposite shear forces. Another important observation is that vertical shear demands for the ties of the DSCW3-3W model are higher than for DSCW3 model. For the DSCW3-3W model, shear demand on the tie-bars is diminished at

regions away from the axis of wall symmetry. These beam forces are below the assumed shear yield strength of the tie-bars, which is roughly 9.3 kips (tie-bars have a 0.63-in. diameter and 50-ksi yield strength).

CONCLUSION

A finite element model previously developed by Polat and Bruneau (2017) and calibrated against experimental results was used here to analyze CFSSP-Walls having different cross-sections and properties in order to investigate more broadly the cyclic inelastic behavior of such composite walls.

Results from re-analyses of previously tested walls with fixed-base boundary conditions (to eliminate any complexity and uncertainty that may arise when including foundation flexibility) were used to obtain tensile axial strain values at
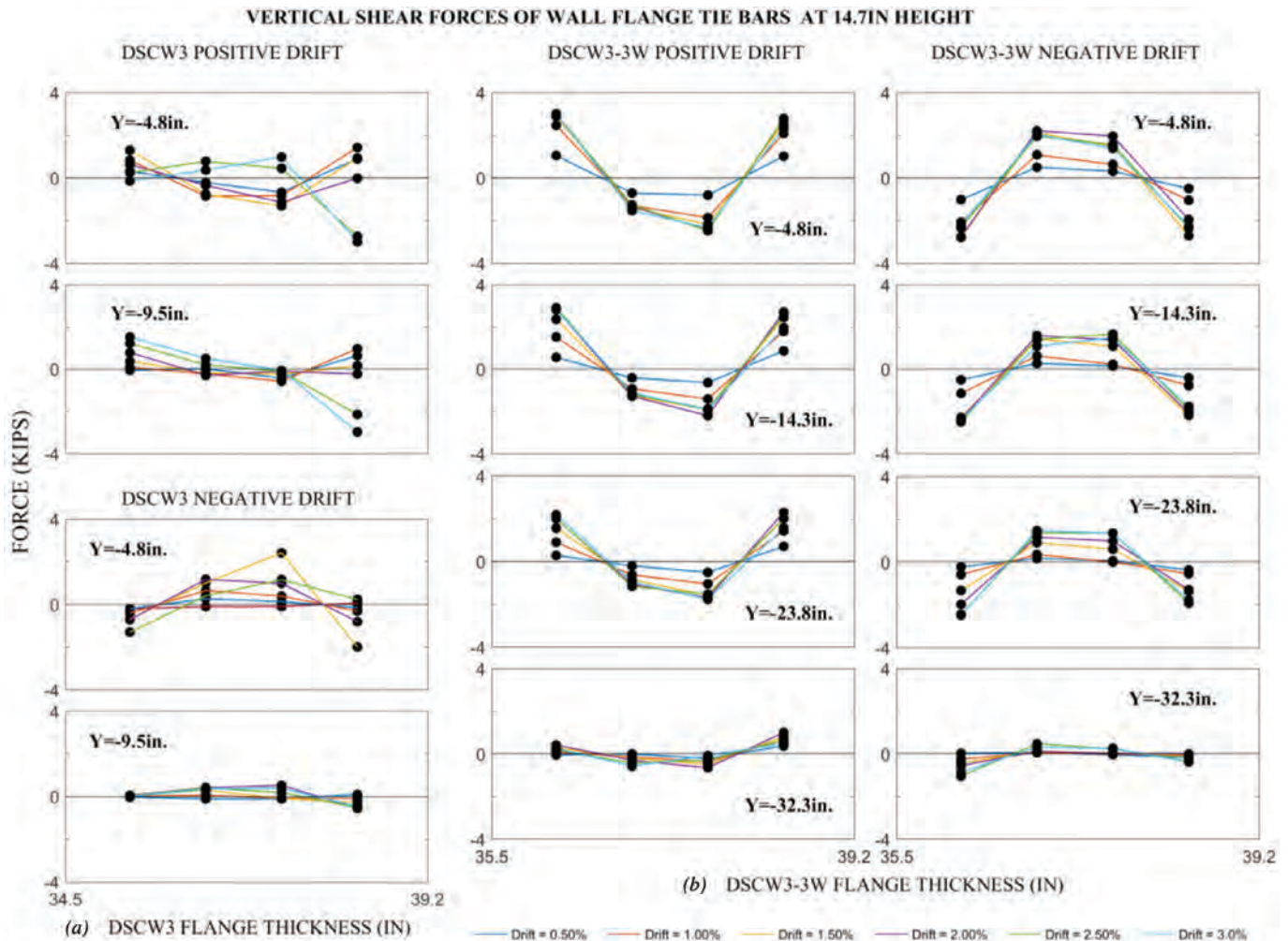

Fig. 26. Vertical shear forces of the wall flange tie-bars at peak drift amplitudes: (a) beam forces of
the DSCW3 model; (b) beam forces of the DSCW3-3W model, under positive and negative drift.

the onset of steel plate buckling, to obtain C_3 values of the concrete, and to estimate the ultimate wall drift that the wall can be sustained under low-cycle fatigue loading without due effect of foundation flexibility.

A parametric study conducted considering different parameters that define CFSSP-Walls, such as D/t, S/t_s and t_c/b, showed that for all cases considered, simple approaches adopted to predict wall plastic flexural strength gives conservative results.

CFSSP-Walls having T-shaped sections were also investigated using the finite element modeling approaches considered throughout. Analyses were performed for a wall tested by Eom et al. (2009), and for a modified configuration having a much greater flange width. Plastic flexural strength of these walls (obtained through simple plastic theory) were shown to be conservative. The modified (increased) flange width of the T-shaped section resulted in the change of the wall compression depths, affected the axial strain demands on the steel web and flange plates, changed the buckling behavior of the steel plates, and reduced the moment contribution of the infill concrete of the wall flange and flange steel plates as a result of reduced axial stress demands. On the contrary, vertical shear forces of the tie-bars located through the thickness of the wall flanges were found to be increased.

ACKNOWLEDGMENTS

REFERENCES

AISC (2016), *Seismic Provisions for Structural Steel Buildings*, ANSI/AISC 341-16, American Institute of Steel Construction, Chicago, IL.

Alzeni, Y. and Bruneau, M. (2014), "Cyclic Inelastic Behavior of Concrete Filled Sandwich Panel Walls Subjected to In-Plane Flexure," Technical Report MCEER-14-0009, Multidisciplinary Center for Earthquake Engineering Research, State University of New York at Buffalo, Buffalo, NY.

Alzeni, Y. and Bruneau, M. (2017), "In-Plane Cyclic Testing of Concrete Filled Sandwich Steel Panel Walls with and without Boundary Elements," *Journal of Structural Engineering*, under review.

Booth, P.N., Varma, A.H., Sener, K.C. and Malushte, S.R. (2015), "Flexural Behavior and Design of Steel-Plate Composite (SC) Walls for Accident Thermal Loading," *Nuclear Engineering and Design*, Vol. 295, pp. 817–828.

Bowerman, H., Gough, M. and King, C. (1999), *Bi-Steel Design and Construction Guide*, British Steel Ltd., Scunthorpe, London.

Epackachi, S., Nguyen, N.H., Kurt, E.G., Whittaker, A.S. and Varma, A.H. (2014), "In-Plane Seismic Behavior of Rectangular Steel-Plate Composite Wall Piers," *Journal of Structural Engineering*, Vol. 141, No. 7, pp. 1–9.

Epackachi, S., Whittaker, A.S., Varma, A.H., and Kurt, E. G. (2015), "Finite Element Modeling of Steel-Plate Concrete Composite Wall Piers," *Engineering Structures*, Vol. 100, pp. 369–384.

Eom, T.-S., Park, H.-G., Lee, C.-H., Kim, J.-H. and Chang, I.-H. (2009), "Behavior of Double Skin Composite Wall Subjected to In-Plane Cyclic Loading," *Journal of Structural Engineering*, Vol. 135, No. 10, pp. 1,239–1,249.

Goto, Y., Kumar, G.P., and Kawanishi, N. (2010), "Nonlinear Finite-Element Analysis for Hysteretic Behavior of Thin-Walled Circular Steel Columns with In-Filled Concrete," *Journal of Structural Engineering*, Vol. 136, No. 11, pp. 1,413–1,422.

Hallquist, J.O. (2006), "LS-DYNA Theory Manual," Livermore Software Technology Corporation, Livermore, CA.

Hibbett, Karlsson and Sorensen Inc. (1998), *ABAQUS/Standard: User's Manual*, Vol. 1.

Imani, R. and Bruneau, M. (2014), "Post-Earthquake Fire Resistance of Ductile Concrete-Filled Double-Skin Tube Columns," Technical Report MCEER-14-0008, Multidisciplinary Center for Earthquake Engineering Research, State University of New York at Buffalo, Buffalo, NY.

Krieg, R. and S. Key (1976), "Implementation of a Time Independent Plasticity Theory into Structural Computer Programs," *Constitutive Equations in Viscoplasticity: Computational and Engineering Aspects*, pp. 125–137.

Kurt, E.G., Varma, A.H., Booth, P. and Whittaker, A.S. (2016), "In-Plane Behavior and Design of Rectangular SC Wall Piers without Boundary Elements," *Journal of Structural Engineering*, Vol. 142, No. 6.

LSTC (Livermore Software Technology Corporation) (2015), "LS-Dyna, Keyword Users Manual," Vols. 1 and 2, Version 971.

Oduyemi, T. and Wright, H. (1989), "An Experimental Investigation into the Behaviour of Double-Skin Sandwich Beams," *Journal of Constructional Steel Research*, Vol. 14, No. 3, pp. 197–220.

Polat, E. and Bruneau, M. (2017), "Modeling Cyclic Inelastic In-Plane Flexural Behavior of Concrete Filled Sandwich Steel Panel Walls," *Engineering Structures*, under review.

Ramesh, S. (2013), "Behavior and Design of Earthquake-Resistant Dual-Plate Composite Shear Wall Systems," Purdue University, West Lafayette, IN.

Schwer, L. (2011), "The Winfrith Concrete Model: Beauty or Beast? Insights into the Winfrith Concrete Model," *Proceedings of the 8th European LS-DYNA Users Conference*, pp. 23–24.

Sener, K. and Varma, A.H. (2014), "Steel-Plate Composite SC Walls: Experimental Database and Design for Out-of-Plane Shear," *Journal of Constructional Steel Research*, Vol. 100, pp. 197–210.

Sener, K., Varma, A.H. and Ayhan, D. (2015), "Steel-Plate Composite SC Walls: Experimental Database and Design for Out-of-Plane Flexure," *Journal of Constructional Steel Research*, Vol. 108, pp. 46–59.

Seo, J., Varma, A.H., Sener, K. and Ayhan, D. (2016), "Steel-Plate Composite (SC) Walls: In-Plane Shear Behavior, Database, and Design," *Journal of Constructional Steel Research*, Vol. 119, pp. 202–215.

SIMULIA (2012), "Abaqus Documentation," Dassault Systemes Simulia Corporation.

Varma, A.H., Malushte, S.R., Sener, K.C. and Lai, Z. (2014), "Steel-Plate Composite (SC) Walls for Safety Related Nuclear Facilities: Design for In-Plane Forces and Out-of-Plane Moments," *Nuclear Engineering and Design*, Vol. 269, pp. 240–249.

Wittmann, F., Rokugo, K., Brühwiler, E., Mihashi, H. and Simonin, P. (1988), "Fracture Energy and Strain Softening of Concrete as Determined by Means of Compact Tension Specimens," *Materials and Structures*, Vol. 21, No. 1, pp. 21–32.

Wright, H.D., Oduyemi, T.O.S. and Evans, H.R. (1991a), "The Design of Double Skin Composite Elements," *Journal of Constructional Steel Research*, Vol. 19, No. 2, pp. 111–132.

Wright, H.D., Oduyemi, T.O.S. and Evans, H.R. (1991b), "The Experimental Behaviour of Double Skin Composite Elements," *Journal of Constructional Steel Research*, Vol. 19, No. 2, pp. 97–110.

Xie, M. and Chapman, J. (2006), "Developments in Sandwich Construction," *Journal of Constructional Steel Research*, Vol. 62, No. 11, pp. 1,123–1,133.

Zhang, K., Varma, A.H., Malushte, S.R. and Gallocher, S. (2014), "Effect of Shear Connectors on Local Buckling and Composite Action in Steel Concrete Composite Walls," *Nuclear Engineering and Design*, Vol. 269, pp. 231–239.